Seismic Investigations of the Nature and Scale of Thermochemical Heterogeneity in Earth's Mantle

by

Samuel McRae Haugland

A dissertation submitted in partial fulfillment
of the requirements for the degree of
Doctor of Philosophy
(Earth and Environmental Sciences)
in the University of Michigan
2019

Doctoral Committee:

Professor Jeroen E. Ritsema, Chair
Professor August Evrard
Associate Professor Eric A. Hetland
Associate Professor Yihe Huang
Adjunct Professor Peter E. van Keken

Samuel M. Haugland
samhaug@umich.edu
ORCID ID: 0000-0003-1415-5241

ACKNOWLEDGMENTS

Any individual accomplishment is nothing other than the sum of the community's collective efforts. I was only lucky to be a part of a outstanding community. Through the years of a graduate degree one runs into many influential professors, staff, and students that shape their intellectual and personal development. First of all, I thank my advisor Jeroen Ritsema for his patience and guidance. This dissertation wouldn't have been possible without his help and advice. I thank Peter van Keken for giving me the opportunity to come to the University of Michigan to study geophysics and for his initial advisorship role. As for the professors, I thank Eric Hetland, Yihe Huang, Gus Evrard, Marin Clark, Kasey Lohmann, Ben Van der Pluijm, Nathan Neimi, and Carlos Chaves. As for the Staff, I thank Anne Hudon, Paula Frank, and Nancy Kingsbury. As Geoclub president I've met too many students to list individually, so I will thank a small subset in particular: Sarah Walker (my girlfriend), Ross Maguire (my closest collaborator), Trever Hines (who taught me Python), Kate Maguire, Kyle Meyer, Joe and Pam el Adli, Mark Robbins, Erin Lynch, Alyssa Abbey, Will Bender, Ian Winkelstern, Marlon Ramos, Prithvi Thakur, Meichen Liu, Billy Medwedeff, Alex Tye, and Maria Rodriguez Mustafa. I've also been fortunate to have a supportive and loving family throughout the process. I thank my parents Brett and Sally and my sister Mackenzie. This research was enabled by National Science Foundation grants EAR-1246700 awarded to Peter van Keken and EAR-1565511 awarded to Jeroen Ritsema.

TABLE OF CONTENTS

LIST OF FIGURES

LIST OF TABLES

ABSTRACT

Thermochemical convection distributes kilometer-scale heterogeneities throughout Earth's mantle. These kilometer-scale heterogeneities, or scatterers, reflect seismic waves which allow us to infer their composition, scale, and distribution. Thermochemical convection also influences the mantle transition zone (MTZ), distorting its topography and potentially leaving signatures of convection patterns in the upper mantle. Understanding mantle heterogeneities at the kilometer scale as well as MTZ topography is a critical component of understanding the nature of mantle convection, which drives all tectonic processes. This dissertation includes three chapters that contribute to our understanding of Earth's mantle.

In chapter 2 I interpret broadband US Array recordings from a 633 km deep South American earthquake as an S-to-P conversion originating from a scattering heterogeneity 1750 km beneath Western Brazil. I model the amplitude and polarity of the signal assuming the heterogeneity is a single scatterer. From the modeling, I show that this block has a characteristic scale length of 10 km and must have a shear velocity slower than the surrounding mantle by up to 12%. This elastic contrast is consistent with the post-stishovite transition of silica, which indicates that the subduction process can entrain and preserve 10 km scale crustal fragments in the deep mantle.

In chapter 3 I construct seismic models of lower mantle structures computed from the mantle convection models of *Brandenburg et al. (2008)* and use them to simulate global observations of PKP scattering. This was the first study to simulate PKP scattering using a joint geodynamic and spectral element waveform simulation method. The results show that simplified incompressible, cylindrical, two-component mantle convection simulations developed to explain geochemical isotope systematics also explain lower mantle scattering.

In chapter 4 I use data from the Arrays of China to recover MTZ thickness beneath the China Sea and surrounding regions by ray-theoretically migrating ScS reverberations. With spectral element waveform simulations I tested the ScS reverberation migration's ability to recover transition zone topography assuming inhomogeneity of sources and 3-D velocity structure. This study revealed that the ScS reverberation migration method is unable to recover degree-20 transition zone topography and that volumetric velocity heterogeneities strongly influence the recovered mantle transition zone thickness.

CHAPTER 1

Introduction

Convection in Earth's mantle drives all tectonic processes at Earth's surface. It distributes kilometer-scale heterogeneities throughout the mantle, modifies mantle composition, and alters the strengths and depths of phase transitions in the mantle transition zone (MTZ). In order to understand the nature of mantle convection, global seismology has proven useful to indirectly probe Earth's interior. Global tomography, broadband waveform modeling, and studies of wave scattering have mapped Earth's interior from 10-km to 1000-km scales and provide some of the best constraints on the temperature, composition, and history of Earth's mantle.

This dissertation is a compilation of three seismological studies informed by numerical simulations of mantle mixing and aimed at uncovering the distribution and composition of small-scale ($\approx$ 10 km) heterogeneity in Earth's mantle. Two published chapters describe studies of P-wave scattering. A third chapter, currently under peer review, concerns the modeling of shear-wave reflections at phase transitions in the MTZ. Figure 1.1 illustrates the three seismic phases covered in these three chapters.

In Chapter 2, I analyze broadband S-to-P converted waveforms recorded by the USArray and produced by a 633-km deep earthquake beneath Western Brazil. Phase conversions are used to identify individual heterogeneities within the mantle. A particular subset of phase conversions is known as the S-to-P conversion, and is commonly used to identify individual heterogeneities beneath deep earthquakes in Wadati-Benioff zones. S-wave energy converts to P-wave energy when encountering any abrupt change in elasticity. The conversion point is uniquely determined by the traveltime, the incidence angle, and azimuth of the incoming wave front and the results are accurate when using 1-D models of seismic wave speed. For this reason, S-to-P conversions have been used to map small-scale seismic structure beneath the Marianas (e.g., *Kaneshima and Helffrich*, 1998), Tonga (e.g., *Kaneshima*, 2013; *Li and Yuen*, 2014; *Yang and He*, 2015), Indonesia (e.g., *Kawakatsu and Niu*, 1994; *Niu and Kawakatsu*, 1996; *Vinnik et al.*, 1998; *Vanacore et al.*, 2006), South America (e.g., *Castle and Van Der Hilst*, 2003; *Kaneshima and Helffrich*, 2010), and Northeast China

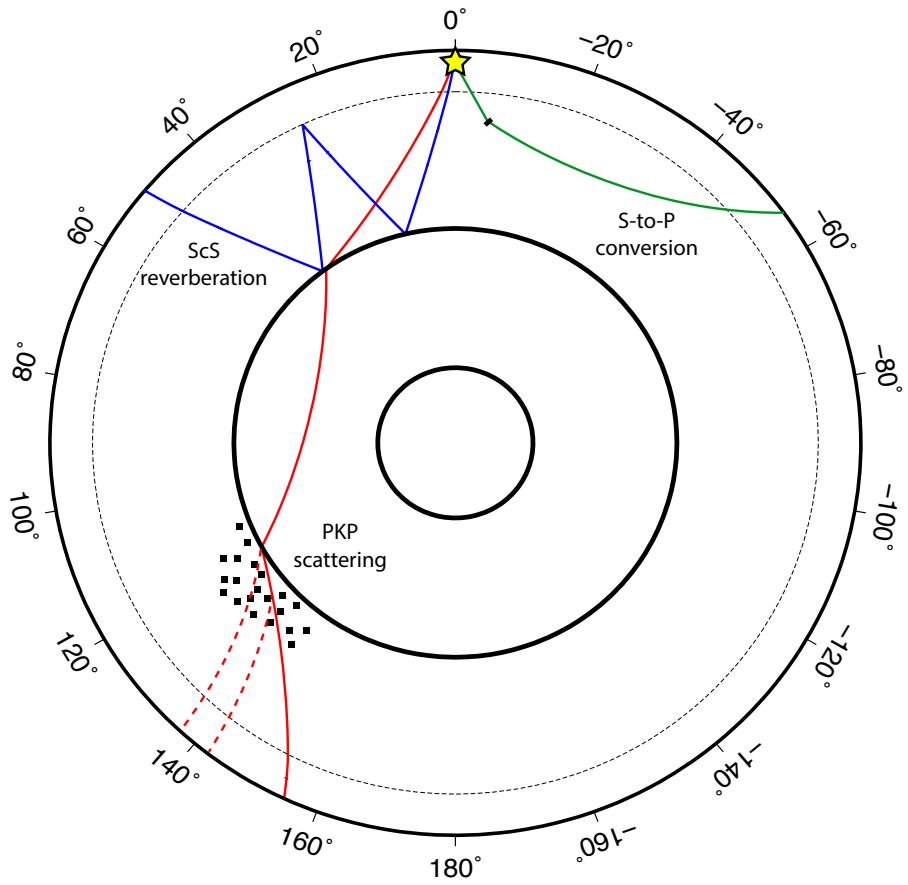

Figure 1.1: Ray-theoretical illustration of three seismic phases covered in this dissertation.

(*Niu*, 2014). *Kaneshima and Helffrich* (1999) interpreted these small-scale, deep mantle heterogeneities as fragments of subducted oceanic crust.

The Brazil earthquake had a dip-slip source mechanism with optimal downward radiation of SV-polarized shear-waves. This focal mechanism provided a unique opportunity to detect a S-wave to P-wave conversion (i.e., S1750P) about 1750 km beneath the Peru/Ecuador border region. The broadband waveform data allowed us to measure the amplitude and polarity of S1750P with greater precision than that of high-frequency recordings used so far. Using full-waveform spectral-element-method modeling, I was able to determine that the heterogeneity producing the S1750P has a characteristic dimension of 10 km and its shear-wave velocity is slower than in the surrounding mantle by up to 12%. This elasticity contrast is consistent with the post-stishovite phase transition thought to occur at mid-mantle conditions (*Tsuchiya*, 2011).

Chapter 3 is a statistical study of global-scale scattering in the lower mantle using PKP

scattered waveforms. Similar to wave conversions, scattering provide a means to study kilometer-scale structures in the deep Earth. However, scattering measurements more appropriate for estimating generalized statistical patterns of small-scale heterogeneity. High-frequency scattered waves are usually recorded over extended time periods and are caused by the interaction of waves with small-scale heterogeneity. For global applications, single scattering theory, or Chernov theory (*Chernov and Silverman*, 1960), is assumed to adequately describe high frequency scattering measurements. Single scattering theory was first applied to earthquake coda by *Aki and Chouet* (1975), and has since been used to model scattering observations of mid-mantle heterogeneity from PP precursors (*King et al.*, 1976) and P'P' precursors (*Haddon et al.*, 1977; *Vinnik*, 1981; *Tkalčić et al.*, 2006), inner core scatterers from PKiKP coda (*Vidale and Earle*, 2000), CMB topography from PKKP precursors *Earle and Shearer* (1997), and lower mantle heterogeneities from Pdiff coda (*Earle and Shearer*, 2001), and PKP precursors (*Haddon and Cleary*, 1974; *Doornbos and Husebye*, 1972).

PKP is a compressional seismic phase that travels through the mantle and outer core and is observed between 145 and 155 degrees. Upon core entry and core exit, kilometer-scale heterogeneities in the lower mantle redirect PKP energy to arrive as incoherent scattering before the PKIKP phase. The intensity and onset time of these arrivals has been used to constrain the statistical heterogeneity in the lower mantle (e.g. *Mancinelli and Shearer*, 2013; *Mancinelli et al.*, 2016). I simulated global PKP scattering observations with full-waveform spectral-element synthetics through Earth models with embedded structures from the geodynamic mantle convection models of *Brandenburg et al.* (2008) (henceforth known as "The Brandenburg models"). These models are relatively simple in their construction, yet reasonably recreate the geochemical isotope systematics of mid-ocean-ridge basalts (MORB) and ocean-island basalts (OIB). In the Brandenburg models, convection is simulated in a 2-D cylindrical domain, where the mantle and core radii are rescaled in order to mimic the curvature of a spherical Earth. This rescaling more accurately approximates heat flow and production for a spherical Earth (*Van Keken*, 2001). The mantle rock is an incompressible binary mixture of eclogite and harzburgite which are represented as tracers that advect within the mantle flow. Despite the cylindrical geometry, incompressibility, and two-component mantle, the surface heat flow and plate tectonic velocities of the Brandenburg models correspond to those of Earth. A suite of Brandenburg models was computed for a range of expected eclogite densities. In models where the eclogite density is significantly denser than the ambient mantle, eclogite tracers pool around the core mantle boundary (CMB) where they are swept by harzburgite-rich subducting slabs. The work of chapter 3 uses the pile and slab structures generated by the Brandenburg models to inform

seismic velocity profiles of the lower mantle in order to simulate global PKP scattering observations. I found that the geometries of convective mantle structures are capable of explaining PKP scattering observations on a global scale.

In addition to distributing kilometer-scale heterogeneity throughout the mantle, convective processes influence and are influenced by mineralogical phase changes in the MTZ. Thermochemical variations caused by subducting slabs to perturb the depth of the 410 km and 670 km discontinuities. Various analyses of P-wave and S-wave reflections (including SS- and PP- precursors) (e.g., *Flanagan and Shearer*, 1998; *Chambers et al.*, 2005; *Schmerr and Garnero*, 2007; *Day and Deuss*, 2013) and P-wave to S-wave conversions (known as receiver functions) (e.g. *Vinnik*, 1977; *Lawrence and Shearer*, 2006; *Jenkins et al.*, 2016; *Maguire et al.*, 2017) at the 410 and 660 km discontinuities have been used to map MTZ thickness undulations due to convective flow in the upper mantle.

In addition underside reflections and P-wave conversions, ScS reverberations are useful for determining the structure of the MTZ between station and earthquake. Chapter 4 describes a new method for the migration of ScS reverberations. ScS reverberations are the class of SH-polarized core reflections ScS_2, ScS_3, sScS, $sScS_2$, and $sScS_3$ and associated top-side and bottom-side reflections off of the MTZ discontinuities. *Revenaugh and Jordan* (1989) were the first to recognize that they can provide constraints on the layering in the MTZ and deep mantle that are complementary to SS and PP precursors and other seismic phases. Numerous studies of the upper mantle followed Revenaugh and Jordan's original work (*Revenaugh and Sipkin*, 1994; *Katzman et al.*, 1998; *Courtier and Revenaugh*, 2006, 2007; *Bagley et al.*, 2013). In these studies, the MTZ and lower mantle between the source-receiver path are modeled as a layered structure of the mantle. I instead develop a common-reflection-point migration technique similar to that of *Wang et al.* (2017) to map the horizontal variations of reflectors in the MTZ beneath the Philippine sea and surrounding regions. I examine the technique's robustness and image artefacts from an analysis of spectral-element method seismograms for several seismic models of the MTZ. The images show MTZ thinning beneath Indonesia and Northeast China, potentially revealing the location of subducted slabs. However, our resolution tests indicate that random degree-20 MTZ thickness variations of 30 km in amplitude are not resolvable by migrating ScS reverberations, likely due to their broad Fresnel zones that render ray-theoretical based migration obsolete. In addition, seismic velocity heterogeneity in the mid-mantle contributes to the recovered MTZ thickness.

1.0.1 Research objectives

The main focus of this dissertation is to use global seismic wave analysis methods to investigate the geographic extent, scale, and elastic properties of subducted material in the deep mantle. I assess whether the distribution of small-scale structures predicted by geodynamic mantle convection simulations scatter PKP energy in a manner consistent with observations. A second aspect of my thesis work is to measure the elasticity and size of an individual fragment of subducted material in the deep mantle. In addition to scattering, I developed a common method for evaluating mantle transition zone topography and appraise its fidelity by reproducing the analysis with 3-D spectral element synthetics.

CHAPTER 2

Estimate of the rigidity of eclogite in the lower mantle from waveform modeling of broadband S-to-P wave conversions. *

Abstract

Broadband USArray recordings of the July 21, 2007 western Brazil earthquake ($M_W = 6.0$; depth = 633 km) include high-amplitude signals about 40 s, 75 s, and 100 s after the P wave arrival. They are consistent with S-wave to P-wave conversions in the mantle beneath northwestern South America. The signal at 100 s, denoted as $S_{1750}P$, has the highest amplitude and is formed at 1750 km depth based on slant-stacking and semblance analysis. Waveform modeling using asymmetric, finite-difference synthetics indicates that $S_{1750}P$ is generated by a 10-km thick heterogeneity, presumably a fragment of subducted mid-ocean ridge basalt in the lower mantle. The negative polarity of $S_{1750}P$ is a robust observation and constrains the shear-velocity anomaly δV_S of the heterogeneity to be negative. The amplitude of $S_{1750}P$ indicates that δV_S is in the range from -1.6% to -12.4%. The large uncertainty in δV_S is due the large variability in the recorded $S_{1750}P$ amplitude and simplifications in the modeling of $S_{1750}P$ waveforms. The lower end of our estimate for δV_S is consistent with ab initio calculations by *Tsuchiya* (2011), who estimated that δV_S of eclogite at lower-mantle pressure is between 0 and -2% due to shear softening from the post-stishovite phase transition.

*Chapter 2 is published in *Geophysical Research Letters*: Haugland, Samuel M., et al. "Estimate of the Rigidity of Eclogite in the Lower Mantle From Waveform Modeling of Broadband S-to-P Wave Conversions." Geophysical Research Letters 44.23 (2017).

2.1 Introduction

While seismic tomography has mapped the penetration of subducting lithosphere into the lower mantle on scales $>$ 100 km (e.g., *Grand et al.*, 1997; *Fukao et al.*, 2001), array recordings of reflected or converted phases indicate fine-scale (10–100 km) structure is present in the deep mantle (e.g., *Shearer*, 2007; *Kaneshima*, 2016). S-to-P conversions at depth x, denoted as SxP, are excellent probes for detecting layering or localized heterogeneity in the lower mantle beneath deep-focus earthquakes. These shear-wave conversions have been used to map small-scale seismic structure beneath the Marianas (e.g., *Kaneshima and Helffrich*, 1998), Tonga (e.g., *Kaneshima*, 2013; *Li and Yuen*, 2014; *Yang and He*, 2015), Indonesia (e.g., *Kawakatsu and Niu*, 1994; *Niu and Kawakatsu*, 1996; *Vinnik et al.*, 1998; *Vanacore et al.*, 2006), South America (e.g., *Castle and Van Der Hilst*, 2003; *Kaneshima and Helffrich*, 2010), and Northeast China (*Niu*, 2014). *Kaneshima and Helffrich* (1999) interpreted these small-scale, deep mantle heterogeneities as fragments of subducted oceanic crust.

We inspected Transportable Array (TA) and Canadian National Seismic Network (CNSN) waveforms from 41 deep-focus ($>$ 300 km) earthquakes in South America since 1990. We detected high-amplitude SxP conversions only in recordings of the July 21, 2007 $M_W = 6.0$ (latitude = 8.1°S; longitude = 71.3°W; depth = 633 km) western Brazil earthquake (the Brazil earthquake from hereon). The Brazil earthquake had a dip-slip source mechanism with optimal downward radiation of SV-polarized shear-waves. The absence of clear S-P conversions in waveform data from other events is likely due to the unique focal mechanism of the Brazil earthquake.

Previous studies have modeled the amplitude and polarity of S-P conversions (e.g., *Vinnik et al.*, 1998; *Kaneshima and Helffrich*, 1999; *Niu*, 2014). In this paper we analyze broadband regional network waveforms by 2D finite difference modeling at periods longer than 2 seconds. The broadband recording of $S_{1750}P$ at stations from the TA and CNSN elucidates the signal polarity and amplitude. By forward waveform modeling, we put constraints on the thickness and the shear velocity of the anomalous structure in the deep mantle responsible for generating $S_{1750}P$.

2.2 SxP conversions in the lower mantle beneath South America

2.2.1 Wave geometry

SxP is formed when the downward propagating S wave converts to a P wave at a discontinuity or heterogeneity in seismic velocity at depth x below the earthquake source. Beneath the Brazil earthquake, SxP conversions form in a high-velocity structure that we interpret as the Nazca lithosphere subducted beneath western South America (Figure 2.1). We can distinguish SxP from crustal reverberations and reflections off boundaries above the earthquake (i.e., p_{410}P, s_{410}P) or beneath the receivers (e.g., P_{410}s, P_{660}s) when its slowness can be determined using recordings from a wide-aperture network.

2.2.2 Waveforms from North America

More than 250 TA and CNSN stations in western North America recorded the Brazil earthquake between 56° and 73°. The record section of vertical-component traces in Figure 2.2a shows the ground velocity after alignment on the P-wave (at time 0). The seismic phases PcP and pP are reflections off the outer core and Earth's surface, respectively. Three S_xP signals at about 45 s, 75 s, and 100 s after the P arrival, are visible throughout the section.

The signals at 45 s, which may interfere with p_{410}P, and at 75 s are S_{950}P and S_{1250}P, respectively. These conversions were formed about 3° off the great-circle path and have complex waveforms. We interpret the impulsive arrival at 100 s as S_{1750}P. Its arrival time decreases with increasing epicentral distance with respect to P, as expected for a SxP conversion.

The vespagram in Figure 2.2b indicates that the slowness of S_{1750}P is about 0.2 s/° higher than predicted for a standard 1-D seismic model. This suggests that the S_{1750}P conversion point is located further from the earthquake hypocenter than expected for a 1-D wave speed model. Semblance is a measure of coherent energy in a stack of data arriving from a common conversion point. By semblance analysis, following *Kaneshima and Helffrich* (2003), we locate the conversion point of S_{1750}P between 1700 and 1750 km depth within the sector of source azimuths of the TA and CNSN stations but about 400 km to the NW of the 1-D predicted conversion location (Figure 2.2c). This is consistent with the S_{1750}P slowness and traveltime observed in Figure 2.2b.

2.3 Waveform modeling

The $S_{1750}P$ signal is recorded above noise level in 30 vertical displacement seismograms from the TA and CNSN. Figure 2.3 shows these waveforms and their sum after they have been aligned and scaled such that the SV wave, which converts into $S_{1750}P$, has an amplitude equal to 1. The $S_{1750}P$ signal in each of these 30 records is comprised of a negative and a positive pulse separated by about 2 s, with varying amplitudes. The mean value of the peak-to-peak amplitude is 4.4% of the SV amplitude on the vertical component and the two-standard deviation of the amplitude is 3.4%.

Computed waveforms indicate that the waveform shape of $S_{1750}P$ is due to the interference of two S-to-P conversions at the upper and lower boundaries of a narrow velocity structure. These two conversions have opposite polarities. We model the heterogeneity that produces $S_{1750}P$ as a block centered on the ray-theoretical $S_{1750}P$ conversion point beneath the earthquake (Figure 2.4a). The block has a thickness h and makes an angle α with the equatorial plane.

We choose long blocks to avoid wave diffraction around them. We expect diffraction to reduce the amplitude of $S_{1750}P$ but it must be studied in 3-D. The S-wave velocity contrast with respect to the ambient mantle is δV_S. Our synthetics indicate that anomalies in the P-wave velocity and density do not affect the $S_{1750}P$ waveform significantly See Figure S2.

We model the stack of the 30 high-amplitude $S_{1750}P$ waveforms using synthetics computed with the PSVaxi method (e.g., *Thorne et al.*, 2013), a finite-difference method similar to the SHaxi method developed by *Jahnke et al.* (2008). PSVaxi allows us to compute the full seismic wavefield of P-SV motions with the correct 3-D geometric spreading for a model of seismic structure in the plane of the great-circle arc. The 2-D grid of heterogeneity is expanded to 3-D spherical geometry by rotating it around the radial axis passing through the seismic source. Our PSVaxi synthetics include signals up to frequencies of 0.5 Hz (i.e., a shortest dominant period of 2 s) but, due to the assumed axisymmetry, signals from off-azimuth wave propagation or SH-to-P conversions cannot be modeled.

We compute synthetics for the PREM seismic model and for a 3-D model in which the block heterogeneity at 1750 km depth is embedded within PREM. In the PREM model, we replace the 220-km, 400-km and 670-km discontinuities by smooth gradients to suppress reflections and conversions produced in the upper mantle. We subtract the PREM and 3-D waveforms to isolate the $S_{1750}P$ signals.

Figures 2.4b and 2.4c compare the recorded $S_{1750}P$ signal (see Figure 2.3c) to synthetic waveforms for different block thicknesses h and shear-velocity anomalies δV_S. The block thickness h controls the travel times of the entry and exit conversions and therefore the

pulse width of $S_{1750}P$. The synthetics for $h = 2$ km and $h = 20$ km clearly underestimate and overestimate the recorded pulse width, respectively (Figure 2.4b). We find the best match for $h = 10$ km and use this value in our modeling. The shear-velocity anomaly δV_S of the block determines the polarity of δV_S. A negative value for δV_S is required to reproduce the down-and-up swing of $S_{1750}P$ (Figure 2.4c).

Figure 2.5 compares the recorded peak-to-peak amplitude of $4.4 \pm 3.4\%$ to predicted amplitudes when varying δV_S (in Figure 2.5a) and block angle α (in Figure 2.5b). The amplitude of $S_{1750}P$ depends linearly on δV_S. A value of $\delta V_S = -7\%$ produces a match between the computed and recorded mean peak-to-peak amplitude of $S_{1750}P$ but values of δV_S between -1.6% and -12.4% match the amplitude within its uncertainty range. The amplitude of $S_{1750}P$ depends on α in a non-linear manner. The predicted $S_{1750}P$ amplitude is highest when $\alpha \approx 10^\circ$. Changing α by 20° decreases the $S_{1750}P$ amplitude by as much as 30%.

2.4 Discussion and Conclusions

If small-scale heterogeneities that produce high-amplitude SxP signals are indeed fragments of mid-ocean ridge basalt (MORB) subducted into the lower mantle, the analysis of SxP waveforms can place important constraints on the elastic properties and composition of MORB at lower-mantle conditions.

There is consensus that the density of MORB is 0.5% to 2% higher than the ambient mantle over the entire lower mantle range (e.g., *Irifune and Ringwood*, 1987, 1993; *Hirose et al.*, 1999; *Litasov et al.*, 2004; *Ricolleau et al.*, 2010; *Irifune and Tsuchiya*, 2015). However, high-pressure experiments on the elastic properties of MORB are challenging and available estimates are based on ab-initio modeling (e.g., *Xu et al.*, 2008; *Tsuchiya*, 2011; *Kawai and Tsuchiya*, 2012; *Kudo et al.*, 2012).

SiO_2 is an important component in MORB and undergoes a phase transition from stishovite to an orthorhombic $CaCl_2$ structure at mid-mantle conditions. *Karki et al.* (1997) first calculated from first principles the elastic parameters of stishovite and $CaCl_2$ and found a decrease in shear velocity. *Tsuchiya et al.* (2004) predicted that silica would exist in the $CaCl_2$ structure at 75 GPa along the geotherm of a subducting slab. If present in subducting slabs, silica will undergo this phase transition and produce seismic heterogeneities commonly observed near subduction zones.

Tsuchiya (2011) estimated that V_S is between 0 and 2% lower than the shear velocity of a pyrolitic mantle at a depth of 1750 km due to a post-stishovite transition. He found V_P does not change appreciably. In contrast, *Xu et al.* (2008) did not include the effect of

post-stishovite and reported that V_S in a pyrolitic mantle increases with increasing basalt fraction. The presence of aluminum in silica further softens both stishovite and $CaCl_2$ (e.g., *Bolfan-Casanova et al.*, 2009; *Lakshtanov et al.*, 2007) Our observation occurs at 75 GPa at a temperature range of 1200–2000 K, well within the P-T conditions of $CaCl_2$ estimated by *Ono et al.* (2002); *Nomura et al.* (2010).

The negative polarity of $S_{1750}P$ is a robust observation and implies that the heterogeneity that produces this arrival has a lower shear velocity than the ambient mantle. The mean amplitude of $S_{1750}P$ indicates that δV_S is between -1.6% and -12.4%. This estimate is uncertain because the recorded $S_{1750}P$ amplitude is highly variable and the modeling is influenced by the geometry and orientation of the heterogeneity. However, the lowest value (i.e., -1.6%) for our estimate of δV_S is consistent with the shear-velocity reduction of MORB at deep mantle pressures, estimated by *Tsuchiya* (2011) as shown in Figure 2.4. We therefore interpret $S_{1750}P$ as a S-wave to P-wave conversion by a small-scale, MORB fragment in a subducted slab in the lower mantle beneath the Brazil earthquake. The relatively low shear-velocity of the MORB fragment is evidence for shear softening due to the post-sitshovite phase transition in MORB in the deep mantle.

Seismological modeling of $S_{1750}P$ can benefit from additional broadband recordings to constrain waveform polarity and amplitude variability. In addition, estimates of the seismic properties of subducted MORB in the lower mantle will improve if we can consider the effects of off-azimuth wave propagation and SH-to-P wave conversions contributing to $S_{1750}P$. This requires computational resources that are currently not available to us.

2.5 Figures - Chapter 2

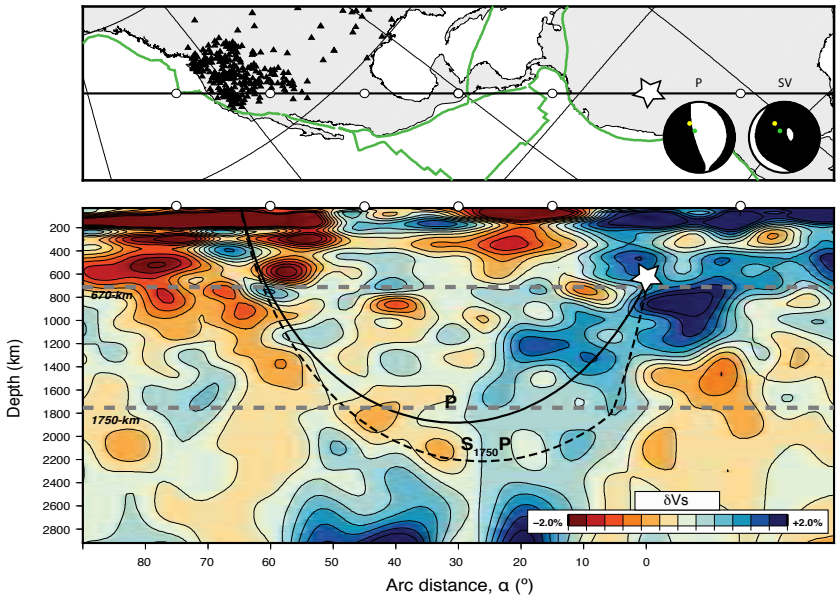

Figure 2.1: (Top) Source-receiver geometry of the July 10, 2007 western Brazil earthquake. The star indicates the epicenter. The triangles indicate the locations of stations from the Transportable Array (TA) and the Canadian National Seismic Network (CNSN) used in the analysis. The black line is great-circle arc through the Brazil event and the western US. The white circles on top are drawn every 15°. P-wave and SV-wave radiation patterns are shown on the lower right. Green circles on the radiation pattern indicate the $S_{1750}P$ take-off direction. Yellow circles on P and SV radiation patterns indicate P and S wave take-off directions, respectively. (bottom) Geometric ray paths of P (solid line) and $S_{1750}P$ (dashed line) for an epicentral distance of 65°. The ray paths are superposed on a NW–SE oriented cross-section of the S40RTS model (*Ritsema et al. (2011)*) through the Brazil event and the TA and CNSN stations. Note that $S_{1750}P$ is formed within a high-velocity anomaly in the lower mantle beneath South America.

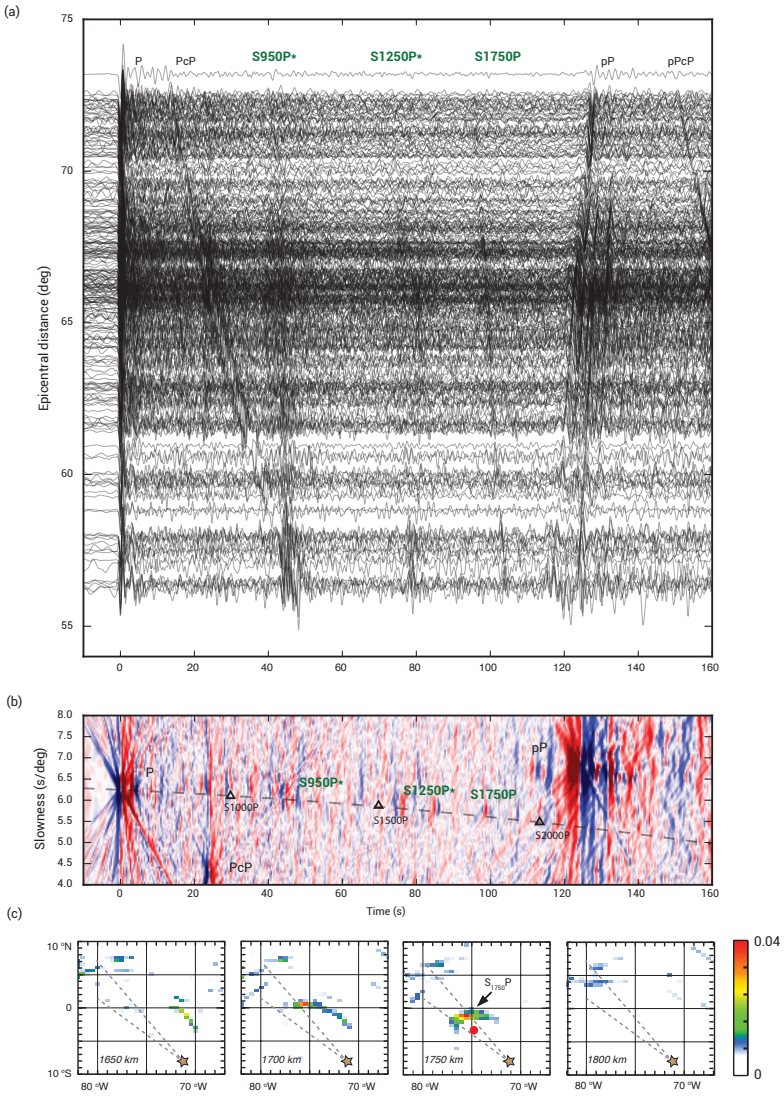

Figure 2.2: (a) Record section of velocity waveforms of the Brazil event aligned on the P-wave arrival (at time 0). Labeled on top are the arrival times of the major phases P, PcP, pP, pPcP, and S-P conversions at 950 km, 1250 km and 1750 km depth. The conversion depths of $S_{950}P$ and $S_{1250}P$ are shallower depth than expected for 1-D models for their traveltimes because these phases propagate off-azimuth for the Brazil earthquake. (b) Vespagram of the absolute amplitude of the sum of waveforms as function of time and signal slowness. The SxP slowness branch is indicated by a dashed line. (c) Map view of semblance coefficients computed for a $0.5° \times 0.5° \times 50$ km grid at 1650 km, 1700 km, 1750 km, and 1800 km depth. The warmest colors indicate where semblance values are the highest. The dashed lines represent the station azimuth range of the TA and CNSN stations with clear $S_{1750}P$ signals. The red circle at 1750 km depth is the $S_{1750}P$ conversion point computed for a 1-D velocity structure.

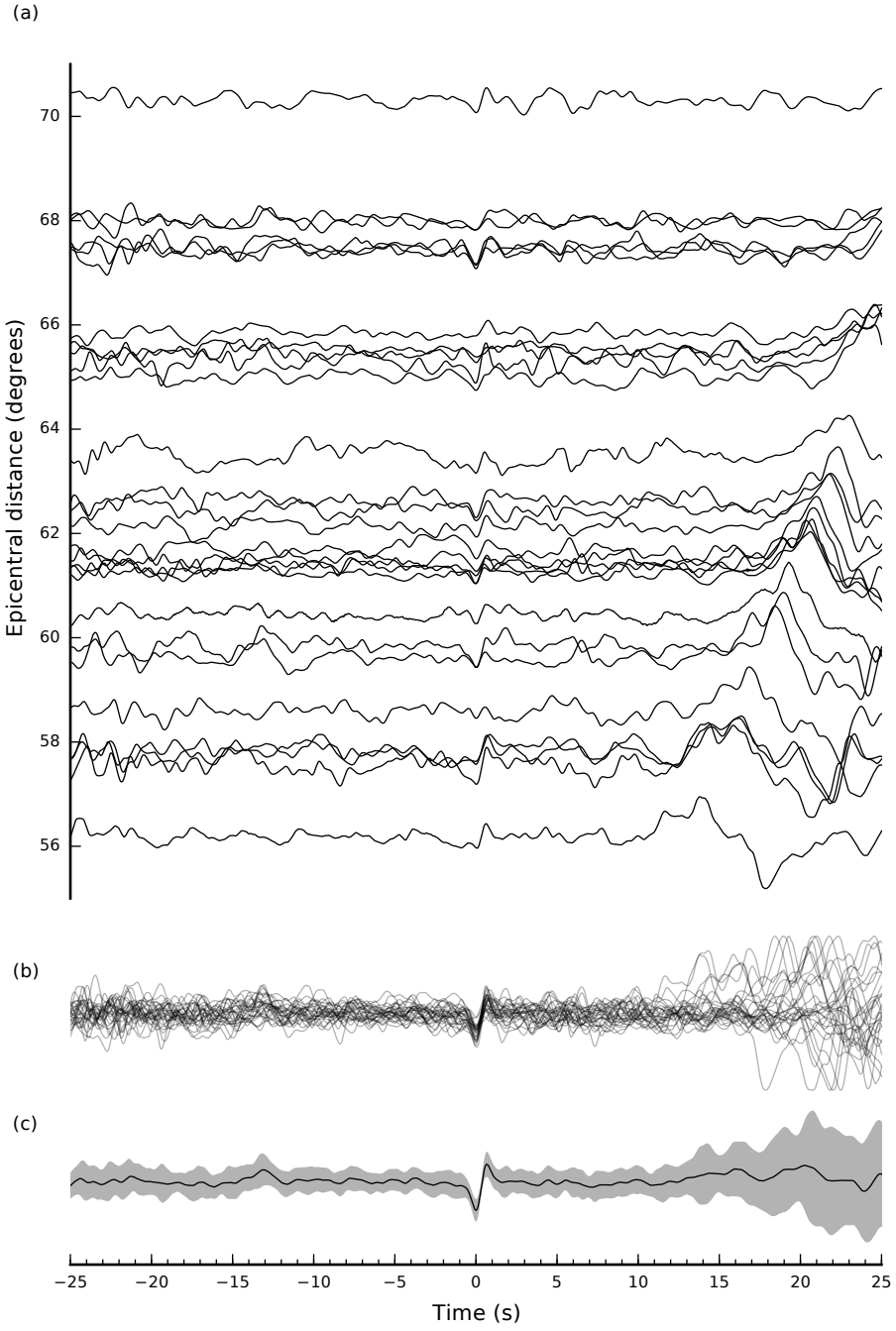

Figure 2.3: (a) Record section and (b) stacked displacement waveforms centered on $S_{1750}P$ from 30 TA and CNSN stations. The large amplitude signal moving out with increasing distance is pP. (c) Sum of the displacement waveforms. The grey envelope is two standard deviations wide and indicates amplitude variability present in the data.

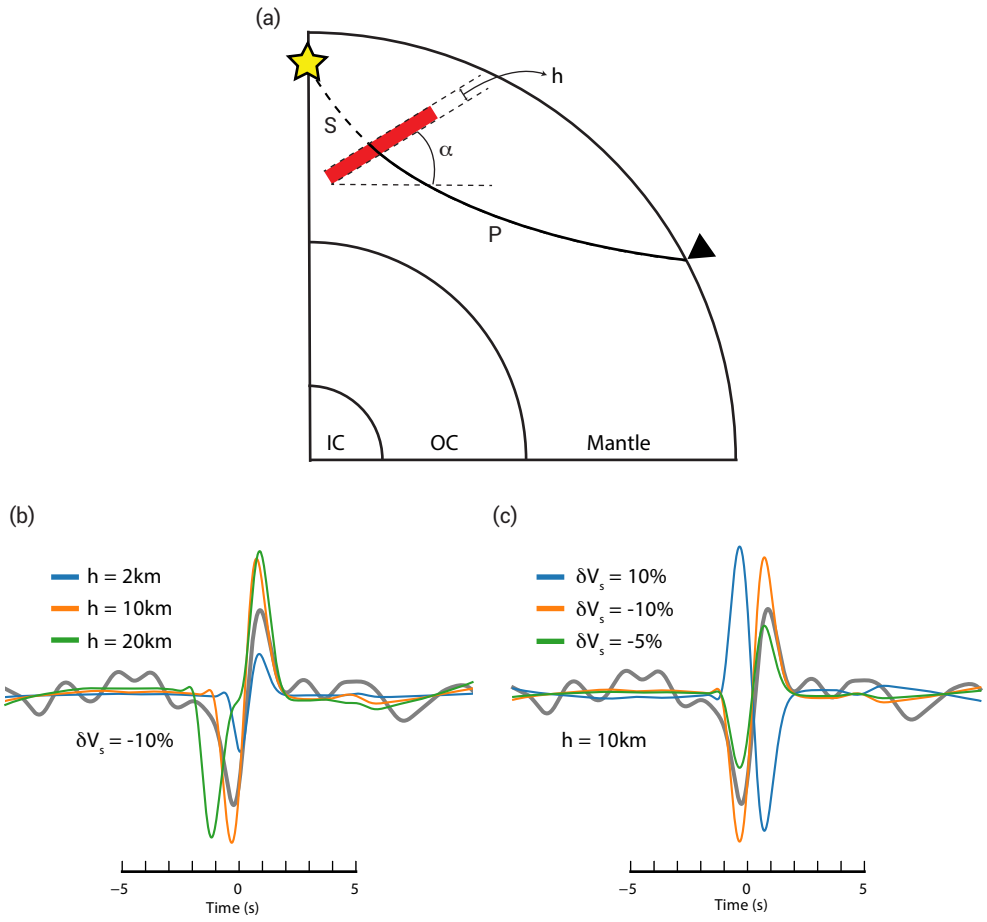

Figure 2.4: (a) Illustration of the model. The heterogeneity responsible for forming $S_{1750}P$ is modeled as a block at 1750 km depth with a thickness h that makes an angle α with the equatorial plane. It has a velocity contrast δV_S with respect to the ambient mantle. (b) Synthetic waveforms for $h = 2$ km, $h = 10$ km, and $h = 20$ km. δV_S = -10% in these simulations. (c) Synthetic waveforms for $\delta V_S = 10\%$, $\delta V_S = -10\%$, and $\delta V_S = -5\%$. $h = 10$ km in these simulations. For all simulations in (b) and (c) $\alpha = 0°$, the epicentral distance is $65°$, and the grey waveform is the stack of the recorded $S_{1750}P$ waveforms.

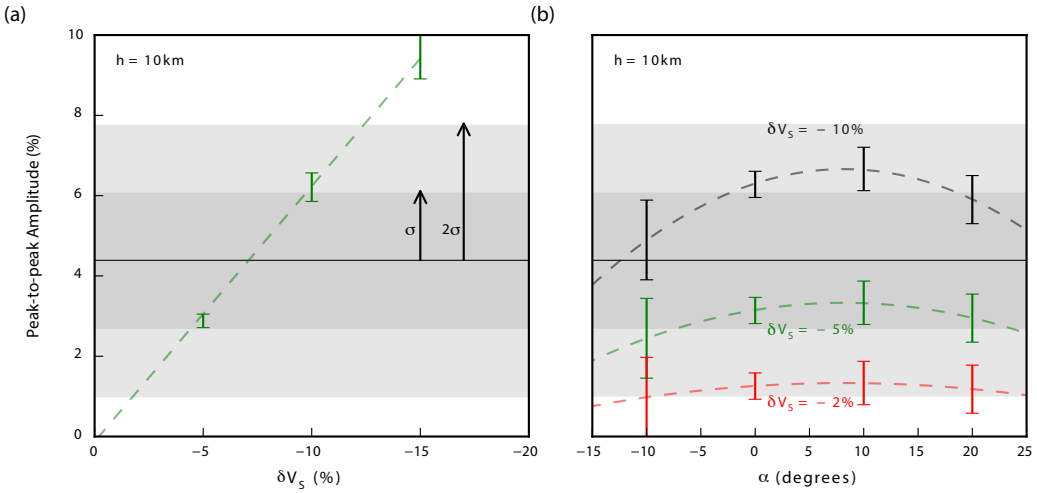

Figure 2.5: Peak-to-peak $S_{1750}P$ amplitude normalized to the radial SV component as a function of (a) δV_S and (b) block angle α. The horizontal black line indicates the mean value of the amplitude. Its two grey envelopes are one- and two-standard deviations wide. Vertical black bars are predicted amplitudes with error bars estimated from the minimum and maximum values for a range of epicentral distances.

CHAPTER 3

Analysis of PKP scattering using mantle mixing simulations and axisymmetric 3D waveforms *

Abstract

The scattering of PKP waves in the lower mantle produces isolated signals before the PKIKP phase. We explore whether these so-called PKIKP precursors can be related to wave scattering off mid ocean ridge basalt (MORB) fragments that have been advected in the deep mantle throughout geologic time. We construct seismic models of small-scale ($>$ 20 km) heterogeneity in the lower mantle informed by mantle mixing simulations from *Brandenburg et al.* (2008) and generate PKIKP precursors using 3D, axisymmetric waveform simulations up to 0.75 Hz. We consider two end-member geodynamic models with fundamentally different distributions of MORB in the lower mantle. Our results suggest that the accumulation of MORB at the base of the mantle is a viable hypothesis for the origin of PKP scattering. We find that the strength of the PKIKP precursor amplitudes is consistent with P wave speed heterogeneity of 0.1–0.2%, as reported previously. The radial distribution of MORB has a profound effect on the strength of PKIKP precursors. Simulation of PKIKP precursors for models with an increasing MORB concentration in the lowermost 500 km of the mantle appears to reproduce most accurately the strength of PKIKP precursors in Global Seismic Network waveforms. These models assume that MORB has an excess density of at least 7%. Additional simulations of more complex geodynamic models will better constrain the geodynamic conditions to explain the significant variability of PKP scattering strength.

*Chapter 3 is published in *Physics of Earth and Planetary Interiors*: Haugland, Samuel M., et al. "Analysis of PKP scattering using mantle mixing simulations and axisymmetric 3D waveforms." Physics of the Earth and Planetary Interiors 276 (2018): 226-233.

3.1 Introduction

Upon entry and exit from the core, small-scale heterogeneity in the lower mantle scatters PKP waves. These scattered waves are called PKIKP (or PKP_{df}) precursors because they are recorded up to 20 seconds before the PKIKP phase between epicentral distances of 120° and 145° (Figure 3.1). PKIKP precursors provide some of the best seismic constraints on the nature of kilometer-scale heterogeneity in the lower mantle (see *Shearer* (2007) for a recent review). *Cleary and Haddon* (1972) and *Haddon and Cleary* (1974) first associated PKIKP precursors with wave scattering by small-scale heterogeneity near the core-mantle boundary (CMB). Following these studies a number of researchers have estimated the strength and scale lengths of small-scale heterogeneity responsible for PKP scattering (e.g., *Bataille and Flatté*, 1988; *Hedlin et al.*, 1997; *Shearer et al.*, 1998; *Cormier*, 1999; *Margerin and Nolet*, 2003; *Thomas et al.*, 2009; *Mancinelli and Shearer*, 2013; *Mancinelli et al.*, 2016), and related PKIKP precursors to CMB topography (e.g., *Doornbos*, 1978), anomalous low wave speed structures at the base of the mantle (e.g., *Vidale and Hedlin*, 1998; *Wen and Helmberger*, 1998; *Wen*, 2000; *Thomas et al.*, 2009; *Frost et al.*, 2013), and subducted slabs (e.g., *Cao and Romanowicz*, 2007; *Miller and Niu*, 2008; *Vanacore et al.*, 2010). Analyses of data from regional (e.g., *Thomas et al.*, 1999; *Wen*, 2000; *Niu and Wen*, 2001; *Yao and Wen*, 2014; *Waszek et al.*, 2015) and global (*Hedlin and Shearer*, 2000) seismic networks indicate that the amplitudes of PKIKP precursors are highly variable. *Hedlin and Shearer* (2000) conclude that PKP scattering is relatively strong beneath central Africa, parts of North America, and north of India, while relatively weak beneath South and Central America, eastern Europe, and Indonesia. Given the sparse sampling of the CMB region by PKP, the relationship between the strength of PKP scattering and the large-scale thermal and compositional heterogeneity in the lower mantle, mapped using seismic tomography, remains unclear.

In this study we estimate the strength of PKP scattering assuming that fragments of mid-ocean ridge basalt (MORB) contribute entirely to PKP scattering. These fragments have been continuously generated and dispersed through the mantle by an assumed 4.5 Byr of mixing by mantle convection. The computer simulations of mantle mixing from *Brandenburg et al.* (2008) inform our of MORB concentration in the lower mantle. We relate the MORB fragments to small-scale P wave velocity anomalies and determine the amplitude variations of PKIKP precursors from spectral-element based waveform simulations *Nissen-Meyer et al.* (2014) at frequencies up to 0.75 Hz. Our hybrid dynamical-seismological approach follows previous joint geodynamic and seismic analyses of wave propagation (*Hwang et al.*, 2011; *Styles et al.*, 2011; *Maguire et al.*, 2016).

3.2 Seismic data and modeling

3.2.1 Stacks of Global Seismic Network waveforms

Following the approach of *Shearer et al.* (1998); *Mancinelli and Shearer* (2013), and *Mancinelli et al.* (2016), we quantify the strength of PKP scattering by small-scale heterogeneity in the lower mantle using stacks of about 20,000 globally recorded seismic waveforms (Figure 3.2). Events with moment magnitude $M_w \geq 5.5$ and hypocenters deeper than 50 km produce the highest quality seismograms. These events are primarily located along the Pacific subduction zones. Most PKP waves cross the CMB beneath the circum-Pacific region. Few PKP waves cross the CMB within the large-low shear velocity provinces in the lower mantle beneath Africa and the Pacific.

The size of our data set, the selection criteria, and signal processing are similar to those in *Mancinelli et al.* (2016), although we are computationally limited to a narrower frequency band. We filter the waveforms using a band-pass Butterworth filter with corner frequencies of 0.4 Hz and 0.75 Hz and discard records for which the ratio between PKIKP and noise level is lower than 5. The traces are aligned on the arrival times of PKIKP and rescaled such that the amplitude of PKIKP is 1 for all waveforms. We stack the envelopes of all seismograms with common epicentral distances within 0.5° wide epicentral distance bins. We analyze seismograms at epicentral distances between 130° and 140°. This is a slightly narrower range than the distance range of 120°–145° considered by *Mancinelli et al.* (2016). We prefer the narrower range because $\mathrm{PKP_{bc}}$ signals overwhelm synthetic PKIKP precursors at epicentral distances larger than 140° and PKIKP precursors have low amplitudes in the 0.4–0.75 Hz frequency window at epicentral distances smaller than 130°.

Figure 3.3 shows the strength of observed PKP scattering. This image shows the amplitude of the stack of waveform envelopes as a function of time and epicentral distance. PKIKP precursors are strongest between 134° and 140°. The time window with precursory signal broadens at distances larger than about 137° but the amplitudes of PKIKP precursors are smaller than 0.1 at more than 7 seconds before PKIKP. This corresponds to the expected arrival time from heterogeneity near 600 km above the CMB and indicates that the signals of PKP scattering in the lowermost 600 km of the mantle are relatively weak in the 0.4–0.75 Hz frequency band, as shown previously by *Mancinelli et al.* (2016).

3.2.2 Numerical simulations of mantle mixing

Our models of small-scale heterogeneity in the lower mantle are derived from the numerical simulations of mantle convection in a 2D cylinder by *Brandenburg et al.* (2008). These

numerical models are based on Boussinesq convection at infinite Prandtl number, a thermal Rayleigh number of $Ra = 5 \times 10^6$, with radiogenic internal heating scaled such that it represents present-day heating by radiogenic elements in the Earths mantle and the estimated effect of present-day secular cooling. The time averaged surface heat flow is similar to the present-day Earth at $\approx 100\ mW/m^2$. The average surface plate velocity is about 3 cm/yr which is similar to the present-day average poloidal speed of plate tectonics. The models are formulated with a simulated form of plate tectonics using force-balanced plates. This sets up energetically-consistent convection with zones of focused convergence and divergence. At the divergent zones basaltic crust is generated by melting of the mantle peridotite, leaving depleted harzburgite below it. Over time the basalt and harzburgitic components are remixed, but the remnants of oceanic crust (represented by black in the left column of 3.4) can remain distinctly embedded in the harzburgite. The basalt turns to eclogite and other phases that are assumed to be either neutral in density with the surrounding peridotite or slightly denser. Crust with excess density $\delta\rho > 0$ tends to accumulate near the CMB forming structures similar to the large low shear velocity provinces that are observed in global tomography (e.g., *Ritsema et al.*, 2011). The continuous extraction of oceanic and continental crust leads to a geochemical evolution that is in broad strokes consistent with the observed trace isotope systems and with the degassing efficiency of the Earth as measured by the amount of ^{40}Ar in the Earth's atmosphere.

We choose two simulations (Table 1) from the *Brandenburg et al.* (2008) study. The MORB concentration C in these simulations have different radial gradients as illustrated in Figure 3.5. The geodynamical models assumed a rescaled core radius which leads to a better representation of heat generation and loss compared to the 3D spherical geometry of the Earth (**?**). In this study we project the temperature and composition determined by the ratio of MORB and harzburgite back onto a cross-section with Earth-like core radius. Table 3.1 summarizes the six models that we will analyze. Simulations A and B are horizontal averages of A_1 and A_2 and of B_1 and B_2, respectively. In simulation A, the MORB fragments are passive because they have no excess density (i.e., $\delta\rho = 0\%$). Their concentration is nearly constant with depth. In simulation B, the MORB fragments have an excess density $\delta\rho = +7\%$ and tend to accumulate in the lowermost 500 km of the mantle. We analyze simulations A and B as 1D profiles, ignoring lateral variations of the MORB distribution.

We also analyze the scattering of PKP waves within regions of the mantle characterized by predominantly downwelling or upwelling flow. Sections A_1 and B_1 from simulations A and B isolate an episode of recent subduction into the lower mantle. The subducted slab has transported relatively wide sections of oceanic crust to the lowermost mantle which form narrow zones of high MORB concentration. These are visible as spikes in C near

the CMB in Figure 3.5. Sections A_2 and B_2 include upwelling from the CMB. In section B_2, fragments of relatively dense MORB have settled into thick piles above the CMB. The MORB concentration in section B_2 therefore increases faster with depth than in simulation B (i.e., the globally averaged MORB structure). On the other hand, the increase in C is smaller for section B_1 because MORB fragments have been swept away by recent subduction.

3.2.3 Waveform simulations

Brandenburg et al. (2008) represented the MORB component by discrete numerical tracers. We use these tracers to define lower mantle small-scale heterogeneity that scatters PKP waves. To reproduce the MORB concentration C as a function of depth, we randomly select 25% of the tracers and assume that each tracer has a 20×20 km^2 volume, the smallest structure to which PKP waves are sensitive at <0.5 Hz, and a $\delta V_P\%$ higher P velocity than the ambient mantle. The δV_P perturbation is with respect to the P wave velocity and attenuation structure in the Preliminary Reference Earth Model (PREM) at a given depth. Since anomalies may overlap, the seismic anomalies have variable dimensions and spacing and a radial distribution of heterogeneity similar to the MORB distribution in Figures 3.4 and 3.5.

To isolate the effects of wave scattering in the downwelling (i.e., sections A_1 and B_1) and upwelling (i.e., sections A_2 and B_2) regions of the mantle, we place P velocity anomalies in the mantle only above the core-exit locations of PKP phase. Further, we omit anomalies in the upper mantle because PKP scattering in the upper mantle would be recorded after the PKIKP onset. We ignore the long wavelength P velocity variations due to the effect of thermal variations on V_P.

We use the AxiSEM method (*Nissen-Meyer et al.*, 2014) (`www.axisem.info`) to compute body-wave seismograms up to 0.75 Hz. AxiSEM honors visco-elastic anisotropic Earth models *van Driel and Nissen-Meyer* (2014a,b), but assumes that the seismic velocity structure has a rotational symmetry about the axis through the poles. We use the PREM model as the background model in all simulations. The earthquake source is a radially oriented monopole with nearly isotropic P radiation in the direction of the PKP and PKIKP waves. AxiSEM waveform simulations run on a 2D numerical section and do not account for out- of-plane scattering. They produce accurate 3D wavefields for 1-D models and models with in- plane lateral heterogeneities. The method is thus appropriate to deliver accurate wave fields for the cylindrical input models delivered by our thermochemical simulations. We analyze arrival times and amplitudes of PKIKP precursors using the same processing

steps as described in section 2.1. We align the synthetics on the peak-amplitude of PKIKP, normalize each trace so PKIKP has an amplitude of 1, and stack waveform envelopes.

To optimize sampling of the heterogeneous mantle (see Figure 3.4) we calculate waveform stacks for four different earthquake locations. By rotating the 2D plane of wave propagation with respect to the source up 15° we attain near-uniform sampling of heterogeneity in the mantle by four bundles of PKP waves. As a consequence, all wave speed anomalies within the mantle sections contribute equally to our simulated images of PKP scattering. As an example, Figure 3.6 shows the waveforms of PKIKP precursors and their stacked envelopes from four AxiSEM simulations with re-positioned events for simulation A. The waveform differences are due to differences in scattering locations but the onset times and overall amplitude character as a function of distance is similar for each of the four simulations.

To simulate traveltime variability due to large-scale wavespeed heterogeneity we stack 4000 envelopes (not shown Figure 3.6) of the same waveform after applying random traveltime shifts to the precursory window (time $<$0 s). The traveltime shifts have a Gaussian distribution with a standard deviation of 1.5 seconds, corresponding to the recorded traveltime variation of PKIKP. The stacking of the slightly time shifted waveforms leads to smooth envelopes of PKIKP precursor waveforms. It does not affect the onset times and amplitude dependence on epicentral distance. In Figure 3.6 we stack four envelopes without traveltime variations to show the effect of envelope smoothing.

3.3 Results

3.3.1 Effect of the strength of P velocity heterogeneity

The results in Figure 3.7 show the effects of variations in P wave velocity perturbations δV_P for simulations A and B on the amplitude of PKIKP precursors. We use $\delta V_P = 0.1$ and 0.2%, with the lower value adapted from the analysis by *Margerin and Nolet* (2003); *Mancinelli and Shearer* (2013). These δV_P values are consistent with mineral physics estimates *Cobden et al.* (2009). To facilitate the comparison with the data stacks from Figure 3.3, we draw contours at PKIKP precursor amplitude 0.04, 0.1, and 0.25 for both the simulations and the data. The velocity perturbation δV_P affects the strength of PKIKP precursors most significantly in simulation A. Precursor amplitude is strongest between 134° and 137° for both A and B as is evident in the shifts of the 0.1 amplitude contours.

For simulation A, we obtained the best match to the recorded strength of PKIKP precursors for $\delta V_P = 0.2\%$, especially near an epicentral distance of 137°. When δV_P = 0.1%

the simulated PKIKP precursors do not have the early high amplitude onset seen in the data at distances larger than $137°$. For simulation B, the strength of the PKIKP precursors depends less strongly on δV_P. This indicates that the radial variation of C (see Figure 3.5) controls the time and distance dependence of the PKIKP precursors more significantly than δV_P.

3.3.2 Effect of MORB distribution

Figure 3.8 illustrates how the strength of PKIKP precursors depend on the assumed value for the excess density $\delta\rho$ of MORB with respect to the ambient mantle. MORB excess density $\delta\rho$ determines its buoyancy and therefore its concentration C in the mantle. In the analysis of the simulations from Table 1 we assume that a MORB fragment corresponds to a P wave anomaly with $\delta V_P = 0.1\%$. The significant differences between the strength of PKIKP precursors between simulations A and B indicate that PKP scattering is strongly influenced by radial gradients in C (see Figure 3.5). For simulation A, in which C does not change with depth, the PKIKP precursors are much weaker than in the data and do not have a clear early onset for distances larger than $136°$. The PKIKP precursors simulated for B, when the MORB concentration increases four-fold in the lowermost mantle, match the amplitude and early high amplitude onset near $137°$ in the data.

For both A and B, the PKIKP precursor amplitudes are larger in the upwelling sections of the mantle (i.e., A_2 and B_2) than the downwelling (i.e., A_1 and B_1) sections of the mantle. Compared to A_1 and B_1, respectively, C is highest in the lowermost mantle for A_2 and B_2. The image of PKIKP precursors simulated for B_2 matches the recorded PKIKP precursors best, indicating that the concentration of small-scale heterogeneity increases strongly in the lowermost 500 km of the mantle. The effect of strong heterogeneity in the lowermost mantle on the onset of PKIKP precursors is apparent when comparing the simulations for A_1 and A_2 with the simulation for A. The narrow spikes in C at the CMB or 200 km above the CMB (see Figure 3.5) produce the early onset of PKIKP precursors in comparison to A.

3.4 Discussion and conclusions

This paper describes initial results of combined geodynamic and waveform modeling of PKP scattering by small-scale heterogeneity in the lower mantle. We have used the mantle circulation simulations from *Brandenburg et al.* (2008) to map advected mid-ocean ridge basalt fragments as P velocity anomalies in the mantle and applied the spectral-element

method AxiSEM (*Nissen-Meyer et al.*, 2014) to determine their effects on high-frequency waveforms. We mapped the strength of PKIKP precursors, reflecting PKP scattering, using the global waveform stacking approach by *Mancinelli and Shearer* (2013) and *Mancinelli et al.* (2016).

Our simulations reproduce the onset time and strength of PKP scattering recorded in global seismic network data at frequencies lower than 0.75 Hz if we assume that P wave anomalies with dimensions of at least 20 km have a velocity contrast of 0.1% with respect to the mantle. This is consistent with previous estimates (e.g., *Margerin and Nolet*, 2003; *Mancinelli and Shearer*, 2013). Models in which the concentration of small-scale heterogeneity increases in the lowermost 500 km of mantle by a factor of 4–5 may reproduce most accurately the recorded onset and amplitude of PKIKP precursors between 130° and 140°. These models are consistent with the accumulation of relatively dense MORB above the core-mantle boundary. PKP scattering is predicted to be particularly strong in regions of the lower mantle where MORB has accumulated into thick piles unperturbed by recent subduction.

Important simplifications of our modeling are, for a large part, due to the limited computational resources available to us. They prohibit a detailed interpretation of our results. Our geodynamic simulations of mantle mixing are based in 2D cylinder geometry by assuming incompressibility. The mantle is assumed to be a mechanical mixture of harzburgite and MORB with a pyrolite composition. It does not include possible contribution to PKP scattering from compositional heterogeneity in the lowermost mantle due to incomplete early Earth differentiation (*Labrosse et al.*, 2007) or the presence of silicate melts (*Williams and Garnero*, 1996).

Our waveform computations are restricted to frequencies lower than 0.75 Hz. This limits us to analyzing heterogeneity with scale lengths larger than about 20 km. Previous studies have demonstrated that PKP scattering is much stronger at frequencies as high as 1 Hz and that heterogeneities responsible for PKP scattering are as small as 10 km (e.g., *Mancinelli et al.*, 2016). Moreover, our waveform simulations ignore out–of–plane scattering which is likely significant in the mantle (*Thomas et al.*, 2009) and is an important component in PKIKP precursors (*Mancinelli et al.*, 2016). Ignoring out–of–plane scattering will underestimate precursor amplitudes. Furthermore, our simulations include only core-exit scattering which may further underestimate precursor amplitudes.

New simulations, also for 3D scattering in 3D models with the novel AxiSEM3D methodology (*Leng et al.*, 2016) or other 3D spectral-element packages (*Komatitsch and Tromp*, 2002) are useful to further explore geodynamic scenarios for the generation and distribution of small-scale heterogeneity in the mantle and address whether or not the dis-

tribution of small-scale heterogeneity in the lower mantle can be used to constrain the dynamics of the mantle.

Table 3.1: Simulations in this study.

Simulation	$\delta\rho$ (%)	Mantle regime
A	0	whole-mantle
A_1	0	downwelling
A_2	0	upwelling
B	+7	whole-mantle
B_1	+7	downwelling
B_2	+7	upwelling

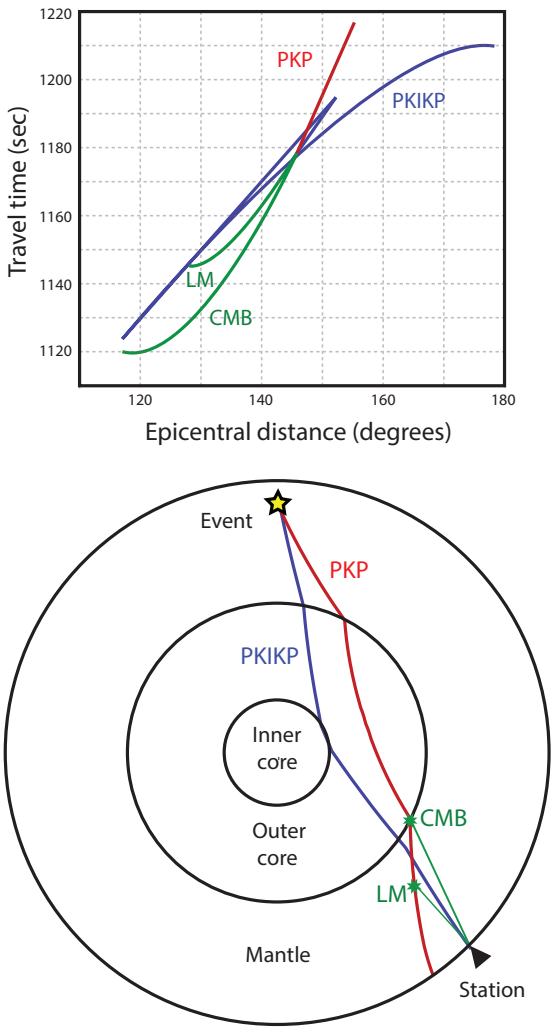

Figure 3.1: (top) Travel time curves of (red) PKP, (blue) PKIKP, and (green) PKP scattered waves as a function of traveltime and epicentral distance. Scattering at the core-mantle boundary (labeled CMB) produces the earliest PKIKP precursors. PKP scattering in the lower mantle (labeled LM) is recorded later. (bottom) Ray paths of PKIKP (blue), PKP (red), and two PKP phases that have been scattered at the CMB and in the lower mantle (green).

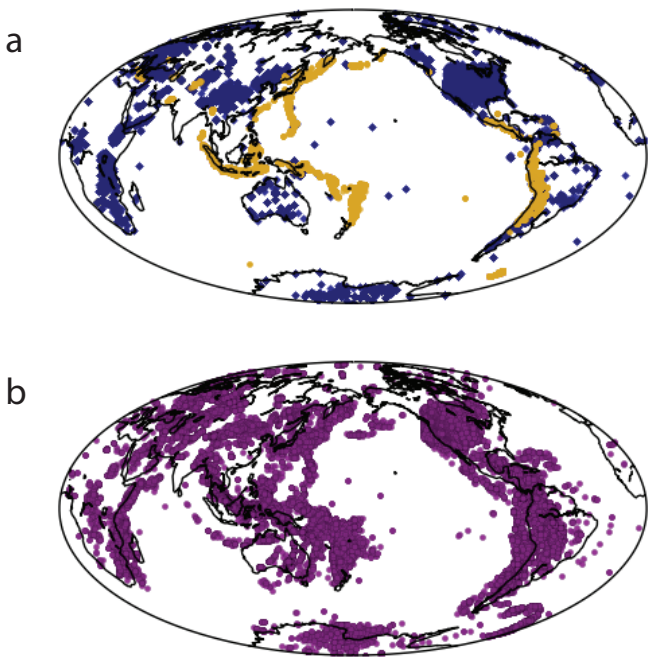

Figure 3.2: (a) Location of events since 1990 (orange) and global and regional network stations (blue) used in this study. (b) Location of the core-exit and core-entry points of PKP.

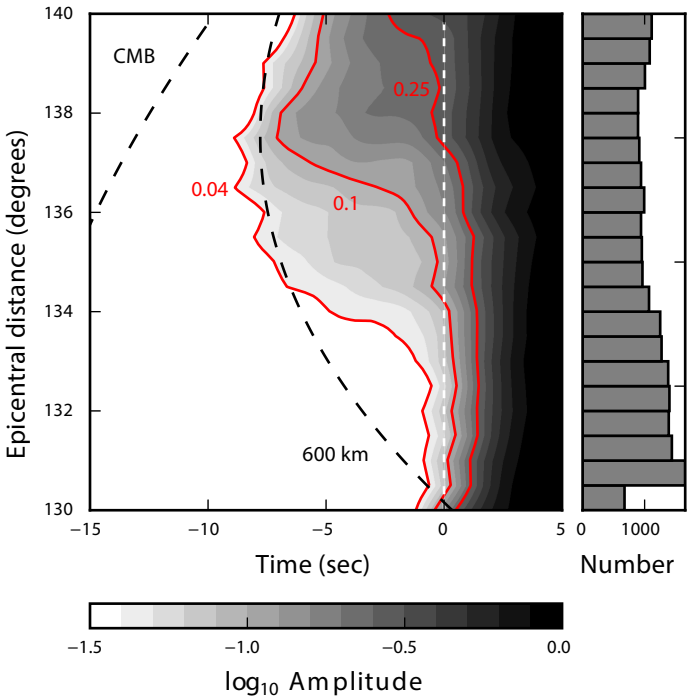

Figure 3.3: Amplitude of observed stacked waveform envelopes as a function of epicentral distance shown using a $\log_{10}$ scale. The stacks are determined for recordings within 0.5 increments of epicentral distance. The histogram on the right indicates the number of envelopes contained in each bin. The amplitude of PKIKP is 1. The three red curves are contours where the amplitudes are 0.04, 0.1, and 0.25. The dashed vertical line at time = 0 marks the onset of PKIKP. The dashed curves indicate the ray theoretical onset time of precursors due to scattering at the CMB and at 600 km above the CMB. See Figure 3.1 for the absolute travel times.

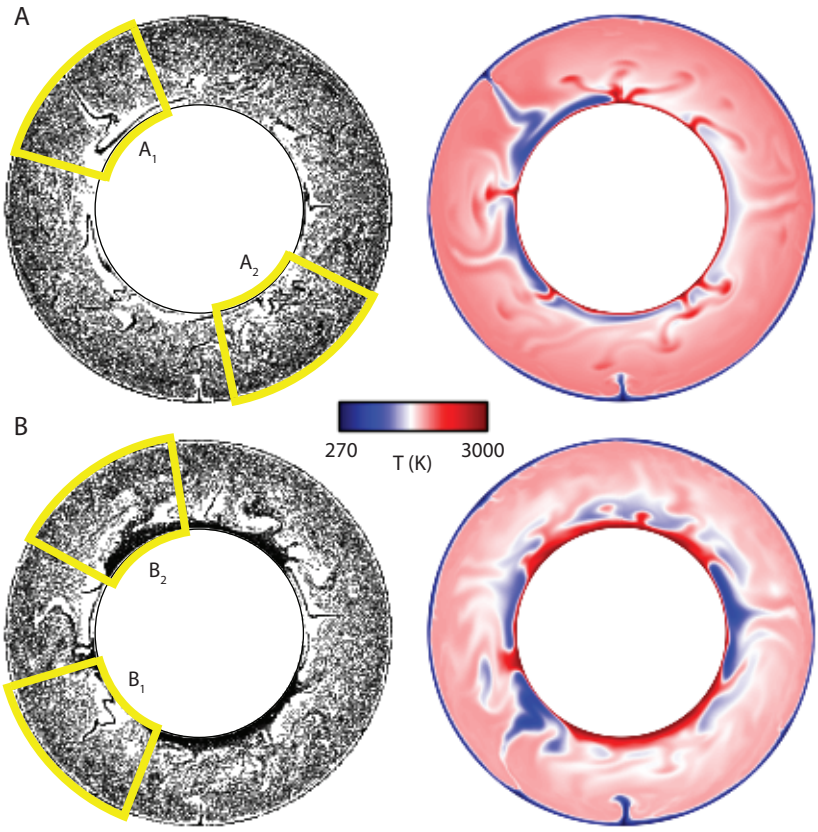

Figure 3.4: Mantle cross-section of simulations A and B from the study by *Brandenburg et al (2008)*. The panels on the left show tracers that reflect the concentration of MORB. The panels on the right show temperature. Simulations A and B differ in the assumed excess density $\delta\rho$ of MORB with respect to the mantle. In A, $\delta\rho = 0\%$. In B, $\delta\rho = +7\%$. The yellow boxes marks regions of the mantle characterized by recent subduction (i.e., A_1 and B_1) or upwelling of the deep mantle (i.e., A_2 and B_2). See also in Table 3.1.

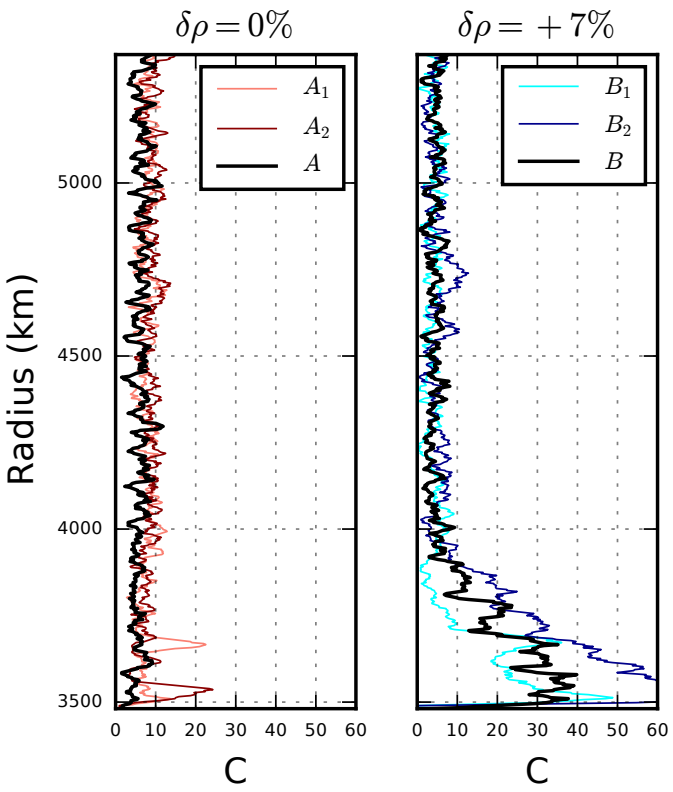

Figure 3.5: Profiles of MORB fraction C (in %) of the mantle as a function of depth for simulations A, A_1, A_2, B, B_1, and B_2. C is defined as the percent mantle volume consisting of MORB tracers in the mantle.

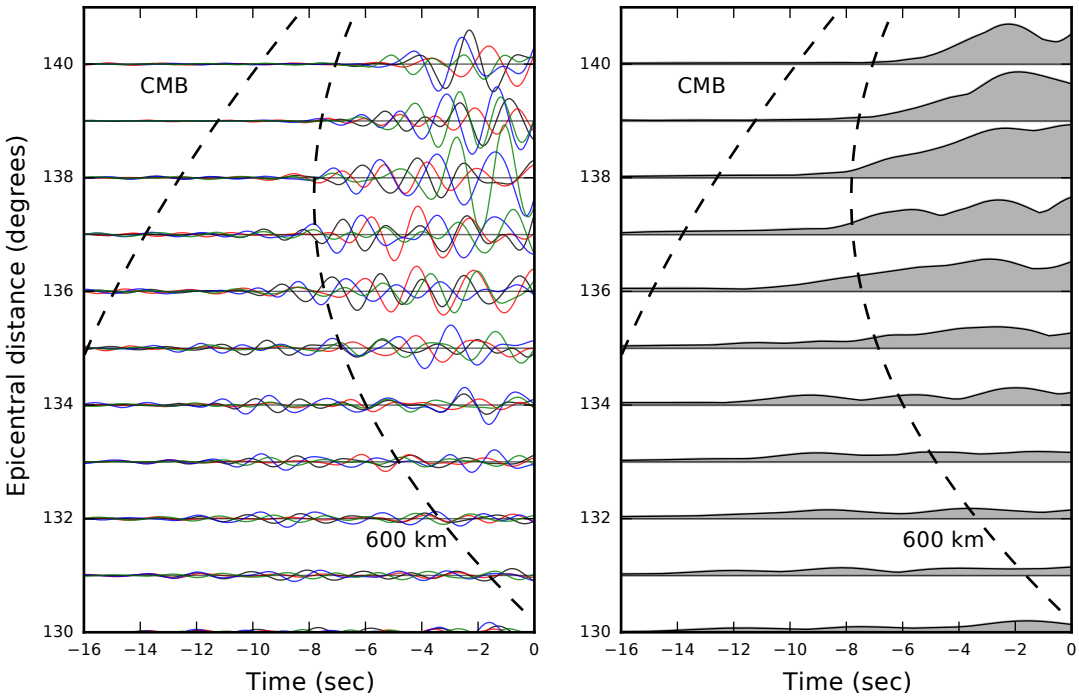

Figure 3.6: Example of AxiSEM waveforms (left) and the waveform envelope (right). The PKIKP onset is at time = 0. Four waveforms (red, green, blue, and black) are computed for MORB profiles in the mantle at four different locations in simulation A. The dashed lines indicate the ray theoretical onset time of precursors due to scattering at the CMB and at 600 km above the CMB.

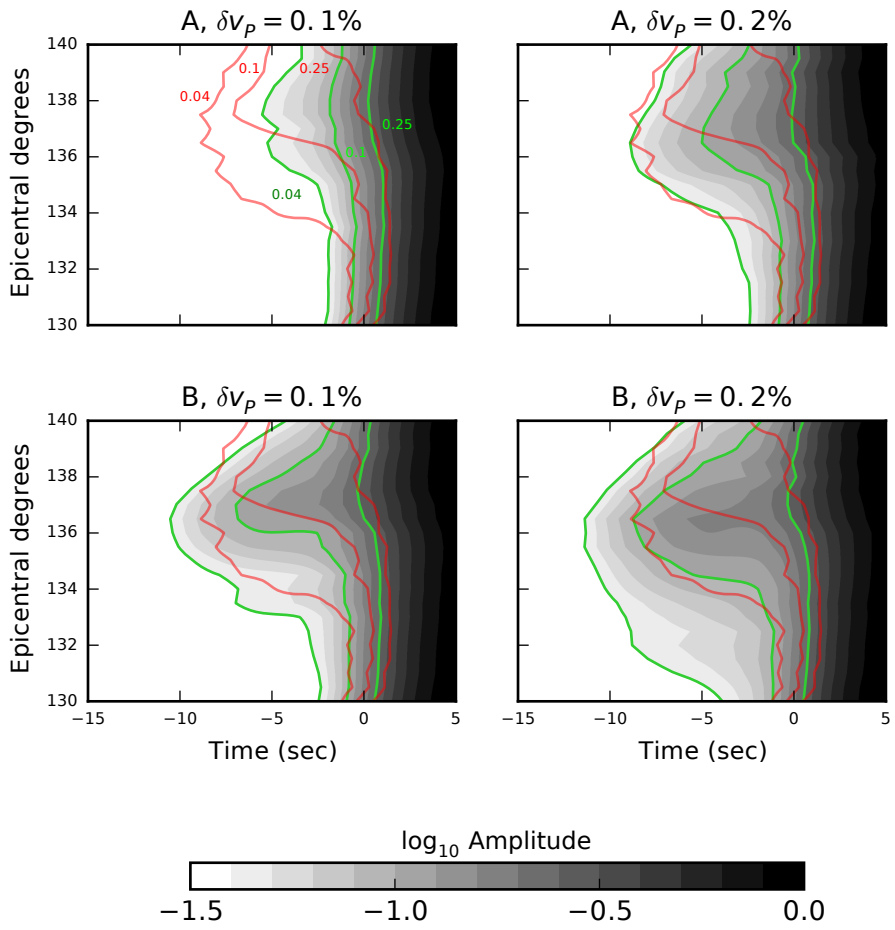

Figure 3.7: Amplitude as a function of arrival time and epicentral distance of PKIKP precursors simulations A (top) and B (bottom) for δV_P = 0.1% (left) and δV_P = 0.2% (right). The PKIKP amplitude is 1 on the PKIKP onset is at time = 0. The green lines are the contours where the amplitudes are 0.04, 0.1, and 0.25. The red lines are contours where the amplitudes in the data are 0.04, 0.1, and 0.25. These are adopted from Figure 3.3.

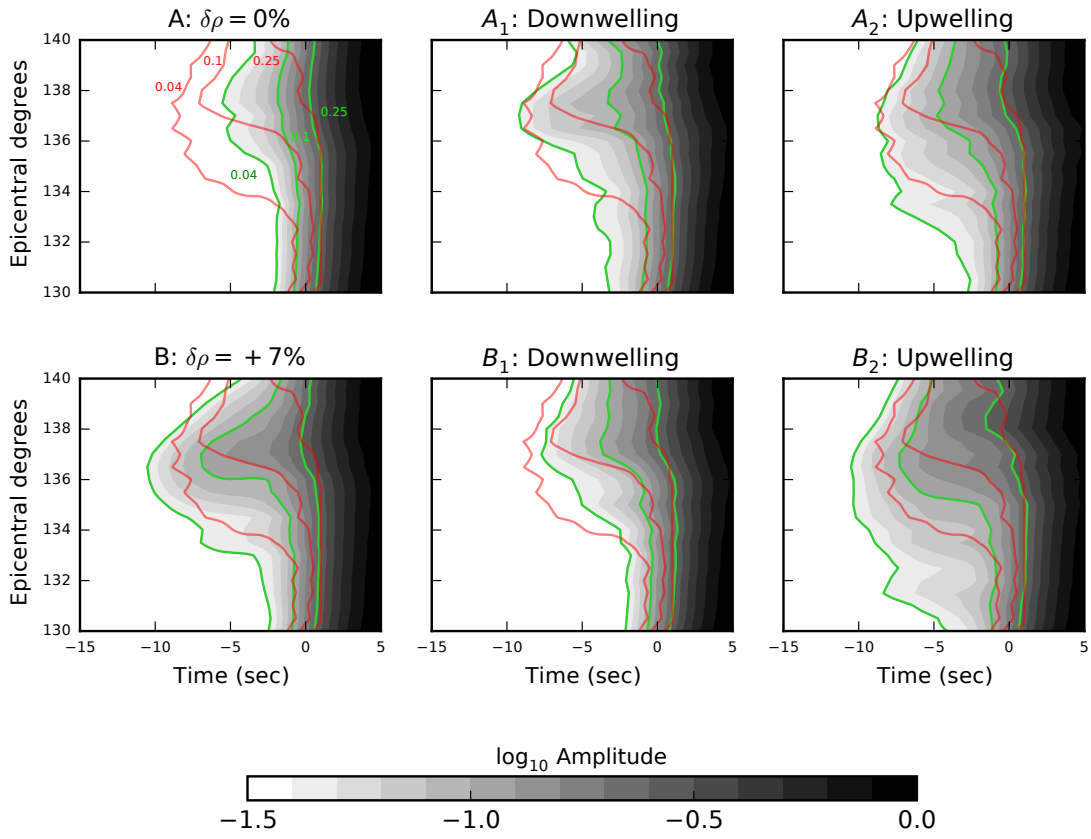

Figure 3.8: Amplitude as a function of arrival time and epicentral distance of PKIKP precursors for simulations A, A_1, and A_2 (top) and B, B_1, and B_2 (bottom). In all cases, $\delta V_P = 0.1\%$. The PKIKP amplitude is 1. The green lines are the contours where the amplitudes are 0.04, 0.1, and 0.25. The red lines are contours where the amplitudes in the data are 0.04, 0.1, and 0.25. These are adopted from Figure 3.3.

CHAPTER 4

Common reflection point mapping of the mantle transition zone using recorded and 3-D synthetic ScS reverberations *

Abstract

We study the mantle transition zone (MTZ) beneath the western Pacific region by analyzing ScS reverberations in the MTZ generated by 36 earthquakes and recorded at hundreds of seismic stations from the combined Arrays of China, Hi-NET in Japan, and Global Seismic Network stations in the region. The analysis involves a 'common reflection point' migration, based on ray-theoretical calculations of reflection points, traveltimes, and slownesses for the PREM model. Our imaging results indicates that the thickness of the MTZ (i.e., the distance between the 410-km and 660-km phase transitions) varies by 20 km and that subduction has modified the thermochemical structure of the MTZ significantly.

Synthetic tests show that the migration approach is robust because the resolved image using PREM synthetics reproduces the PREM structure almost perfectly. However, our analysis of seismograms computed for 3-D models indicate that a ray-theoretical interpretation long-period ScS traveltimes is inaccurate. ScS reverberations appear to be insensitive to degree-20 topography on the 410 and 660. The strong influence from shear-velocity structure is evident from the migration of synthetics for the S20RTS velocity model and the form of the sensitivity kernel of the phase ScS_2 at a period of 15 s. We suspect therefore that the projection of global-scale velocity structure into phase transition topography affect the quality of our image of the MTZ beneath the western Pacific region.

*Chapter 4 is under review for publication in Geophysical Journal International.

4.1 Introduction

The phase transitions from olivine to wadsleyite at about 410 km depth (the '410' from here on) and from ringwoodite to bridgmanite and ferropericlase at 660 km depth (the '660' from here on) produce the strongest seismic discontinuities in the mantle transition zone (MTZ). Since the depths of the 410 and 660 depend on temperature and composition, the thickness of the MTZ, defined as the distance between the 410 and 660, has been measured frequently to study the dynamics of the mantle. See *Deuss* (2009) and *Kind* (2007) for recent reviews.

A variety of seismic data have been used to study the MTZ including triplicated waveforms (e.g., *Grand and Helmberger*, 1984; *Song and Helmberger*, 2006; *Stähler et al.*, 2012), underside P-wave and S-wave reflections off the 410 and 660 (the so-called PP and SS precursors) (e.g., *Flanagan and Shearer*, 1998; *Chambers et al.*, 2005; *Schmerr and Garnero*, 2007; *Day and Deuss*, 2013), and P-wave to S-wave conversions at the 410 and 660 (e.g. *Vinnik*, 1977; *Lawrence and Shearer*, 2006; *Jenkins et al.*, 2016; *Maguire et al.*, 2017).

In this paper we focus on the analysis of the MTZ using the phases ScS_2, ScS_3, sScS, $sScS_2$, and $sScS_3$ and associated top-side and bottom-side reflections off discontinuities in the mantle, including the 410 and 660. These reflections are collectively called ScS reverberations. *Revenaugh and Jordan* (1989) were the first to recognize that they can provide constraints on the layering in the MTZ and deep mantle that are complementary to SS and PP precursors and other seismic phases. Numerous studies of the upper mantle followed Revenaugh and Jordan's original work (*Revenaugh and Sipkin*, 1994; *Katzman et al.*, 1998; *Courtier and Revenaugh*, 2006, 2007; *Bagley et al.*, 2013). In these studies, the MTZ and lower mantle between the source-receiver path are modeled as a layered structure of the mantle. We instead use a common-reflection-point migration technique similar to that of *Wang et al.* (2017) to map the horizontal variations of reflectors in the MTZ beneath the Philippine sea and surrounding regions. We apply it to waveform data for 36 earthquakes recorded at hundreds of seismic stations in China, Japan, and Indonesia. We examine the technique's robustness and image artefacts from an analysis of spectral-element method seismograms for several seismic models of the MTZ.

4.2 Methods

4.2.1 Reverberation modeling

In a low-pass filtered ($T > 15$ s) transverse-component seismogram, the phases ScS_2, ScS_3 and the depth phases sScS, $sScS_2$, and $sScS_3$ are typically recorded above noise level for relatively strong ($M_W > 7$) earthquakes at epicentral distances up to 80°. Figure 4.1 shows a representative example of recordings we have examined in this study. The main phases arrive between 500 and 3600 s after the earthquake origin time. Their amplitudes decrease with increasing arrival time due to geometric spreading and attenuation. No other major teleseismic phases have the same traveltimes but trailing Love waves can interfere with sScS and ScS_2 especially for shallow earthquakes.

Low-amplitude arrivals between the main phases are reflections from discontinuities in the MTZ. We define five reverberation windows between the main and depth phases with energy from these reflections. Signals arriving within 250 s before ScS_2 and ScS_3 and within 250 s after sScS, $sScS_2$, and $sScS_3$ are bottom-side and top-side reflections, respectively. Only ScS_2 and its bottom-side reflections in window 2 reflect once and exactly midway between source and receiver. In a 1D reference Earth model, reverberations within windows 1, 3, 4, or 5 can propagate with the same traveltimes along different paths. This traveltime degeneracy disappears when the seismic structure of the mantle varies laterally.

Since the ScS reverberations have low amplitudes, we use the method by *Schultz and Gu* (2013) to improve their signal-to-noise ratio and to suppress interfering Love waves. Similar to *Wang et al.* (2017), we deconvolve signals in each of the five intervals by the corresponding main phases to remove the effects of earthquake finiteness on the waveforms. This allows us to combine earthquakes with different source durations but the deconvolution may produce spurious side-lobes above and below the 410 and 660 reflections. By ray tracing through the PREM velocity structure we calculate the reflection points and arrival times of the ScS reverberations relative to the main phases.

4.2.2 Potential migration artefacts

Our migration procedure has two intrinsic limitations even for the simplest cases. At first, as mentioned in section 2.1, top-side and bottom-side reflections at different discontinuities can have the same traveltimes. Hence, reflection points cannot be determined uniquely without perfect data coverage. As an example, we consider an earthquake at a depth of h km and the following two phases: (i) the top-side reflection at a discontinuity at d km depth below the seismic station (Figure 4.2a) and (ii) the top-side reflection of a boundary at x

km depth near the earthquake source (Figure 4.2b).

For a receiver side reflector at a depth of $d = 660$ km, we write the two reflections using TauP notation (*Crotwell et al.*, 1999) as ScSSv660S and sSvxSScS, respectively. They have the same traveltimes for unique combinations of x and h (Figure 4.2c). For an earthquake at the surface (i.e., $h = 0$), $x = 660$ km and the ray paths are mirror images. When h is larger than 200 km, the traveltimes of ScSSv660S and sSvxSScS are identical only if x is smaller than 410 km. When h is smaller than 200 km, the two phases have the same traveltimes for values of x between 410 km and 660 km, i.e., for reflections in the MTZ. For a receiver side reflector at a depth of $d = 410$ km, the traveltimes of ScSSv410S and sSvxSScS are the same only for source-side reflections at $x < 410$ km and source depths $h < 410$ km. To image the MTZ, and the 410 and 660 in particular using ScS reverberations, it is best to avoid earthquakes between 180 km and 220 km.

The second limitation pertains to the theoretical simplifications made to calculate reflections points and traveltimes. In addition to the trade-off between the velocity structure in the MTZ and the depths of the 410 and 660, shear-velocity anomalies throughout the mantle may be projected as undulations on the 410 and 660 because of the broad sensitivities of ScS reverberations to seismic structure in the mantle. This limitation will be discussed in more detail in Section 4.

4.3 Application to data

We use 36 events since 2009 with magnitudes between 6 and 8 and depths between 150 and 670 km (Table 4.1). These events occurred in the subduction zones of Sumatra, Java, and the western Pacific (Figure 4.3a). We use waveform data from the Arrays of China, comprised of 30 regional networks across mainland China with a total of 840 stations. In addition, we use data from the broadband Hi-net array in Japan and GSN stations in the region to expand azimuthal coverage. We obtain transverse-component velocity records by rotating the N/S and E/W component record. We low-pass filter these at periods longer than 15 s to maximize the signal-to-noise ratio of the ScS multiples.

4.3.1 Migration results

Figure 4.4 shows the map and histograms of the thickness of the MTZ obtained after applying our migration procedure to waveforms from earthquakes in Table 4.1. The mean MTZ thickness inferred from global data is on average 250 km thick (*Flanagan and Shearer*, 1998), with maximum perturbations of 20 km. In the study region, the MTZ is thinnest

beneath southern China and the Pacific Ocean south of Japan. It is thickest beneath northeastern China, Indonesia, the Philippine Sea, and the Pacific Ocean east of the Philippines, consistent with plate subduction. The widening of the MTZ beneath northeastern China has also been inferred from receiver function studies by *Li and Yuan* (2003), *Ai et al.* (2003), and *Shen et al.* (2008). The presence of a cold slab near the base of the MTZ can explain discontinuities below the 660 due to the ilmenite to perovskite transformation (*Niu and Kawakatsu*, 1996; *Gao et al.*, 2010). The wide MTZ beneath the Indonesia is consistent with the receiver function study by *Saita et al.* (2002) and a study of ScS reverberations by *Ohtaki et al.* (2002), both based on waveform data from the JISNET array.

Figure 4.5 shows depth slices of the migration image along cross sections A–A' and B–B'. We do not show the image for depths shallower than 200 km and deeper than 800 km where artefacts from the migration are strong. The 410 and 660 are conspicuous boundaries but the amplitudes vary laterally. The negative polarity signals just above and below are most likely side-lobes due to signal deconvolution. Two boundaries near 280 km and 500 km depths are also coherent features. The boundary near 500 km depth may be associated with the wadsleyite to ringwoodite phase transition. The partition into two signals may have the same origin as the splitting of the 520-km discontinuity observed by *Deuss and Woodhouse* (2001) in SS precursors. The boundaries near 280 km depth is likely the result of energy reflected from the 410 mapping to shallower depths (Figure 4.2).

4.4 Synthetic tests

In this section we examine the quality of the migration results illustrated in Figures 4.4 and 4.5. We investigate in particular the effect of ray theoretical calculations of traveltimes on the migration results, motivated by our previous analysis of the traveltimes of long-period body waves through a 3-D mantle (*Bai et al.*, 2012; *Koroni and Trampert*, 2015; *Chaves and Ritsema*, 2016).

We apply the migration approach described in Section 2 to seismograms computed with the spectral element method (*Komatitsch and Tromp*, 2002). We consider 13 of the 36 earthquakes indicated with asterisks in Table 4.1 to minimize computational cost. We compute waveforms for a dense and homogeneous grid of stations (Figure 4.3b) to optimize data coverage.

We explore three Earth models. The first model is PREM in which wave speed varies with depth and the 410 and 660 are at depths of 400 and 670 km, respectively. PREM has an additional discontinuity at 220 km depth but no discontinuities within the MTZ. The second model, called PREM-D, has the PREM velocity structure but we add opposite

topography on the 410 and the 660 such that the thickness of the MTZ has a random degree-20 structure with peak-to-peak variations of up to 30 km (Figure 4.6). In the third model, called PREM-V, the 410 and 660 are horizontal and at 400 km and 670 km depth as in PREM but the velocity structure is the degree-20 velocity structure of tomographic model S20RTS (Figure 4.7).

Figure 4.8 shows the migration results for the PREM model for two different waveform sets. In the first set (Figure 4.8a,b,c) we migrate the waveforms of all 13 earthquakes. As in Figure 4.4, we show the map and histograms of the MTZ thickness. The resulting image features a transition zone with a median thickness of 272 km, which is 2 km thicker than in PREM. The thickness of the MTZ varies by less than 10 km. Both the 410 and 660 are clearly resolved but the 660 is stronger. We attribute the relative weak 410 to destructive interference as energy from the 660 is erroneously projected near the 410 because waveforms from event 24 at a depth of 208 km are included in the analysis. Both the 410 and 660 are surrounded by negative side lobes which originate from same signal deconvolution that we also apply here.

In the second set (Figure 4.8d,e,f), we exclude waveforms from the 4 earthquakes shallower than 220 km depth, including event 24. The image is now more precise for the reasons discussed in Section 2. The resolved thickness of the MTZ varies less and the 410 is more pronounced. Our tests demonstrate that the migration procedure is robust since we reproduce a MTZ structure similar to PREM with artificial variations of the MTZ thickness smaller than about 2 km.

The migration of waveforms computed for model PREM-D (Figure 4.9) produces a transition zone with a median thickness of 272 km. Interestingly, this is closer to the PREM MTZ thickness of 270 km than the migration image based on the PREM waveforms. The resolved variation of the MTZ thickness of about 2 km is slightly wider than the variation resolved for PREM. The horizontal pattern of the MTZ thickness is not the same as in PREM-D and the maximum 2-km perturbations from the mean MTZ thickness grossly underestimates the 30-km prescribed variation in PREM-D (Compare Figures 4.6 and 4.9). This indicates that the ScS multiples are insensitive to the degree-20 variations of the MTZ thickness.

The image obtained from migrating PREM-V synthetics (Figure 4.10) features a median thickness of the MTZ of about 265 km. This is 5 km less than the PREM value because overall the shear velocity is relatively high in the MTZ beneath the study region for model PREM-V. The MTZ thickness varies by about 5 km, which is more than resolved for the PREM and PREM-D models. There is no obvious correlation between the resolved MTZ thickness and S20RTS shear velocity structure in the MTZ (i.e., Figure 4.10a versus Figure

4.7b)). Therefore, the degree-20 velocity structure of S20RTS projects as stronger variation in the MTZ thickness than the degree-20 thickness variations of PREM-D.

4.5 Discussion and Conclusions

We have applied a common reflection point migration technique to seismic boundaries in the MTZ using 21,307 ScS reverberation waveforms from regional and global network stations in eastern Asia. In agreement with previous studies based on SS precursors and mantle receiver functions we resolve a complex structure that suggests significant modification of the western Pacific mantle by dynamic processes.

The thickness pattern correlates well with subduction patterns throughout the region. Our image suggests that the mantle transition zone beneath the western Pacific has an average thickness of 250 km and varies by as much as 15 km. Variations in the thickness of the MTZ appear consistent with the presence of relatively cool slabs and their effect on the 410 and 660 phase transitions.

Our analysis of PREM synthetics shows that the methodology is robust. The 410 and 660 km discontinuities are resolved at the expected depths and with the expected relative strengths. Even in this simple case, the imaged MTZ thickness varies up to 2 km. These small variations are due to traveltime measurement inaccuracies and inhomogeneous earthquake distribution.

Previous theoretical and forward modeling studies have demonstrated that ray theory may not be useful for the modeling of long-period body waves. In the case of SS precursors, ray theory underestimates traveltime delays by up to factor of two (*Bai et al.*, 2012) because these long-period waves are sensitive to structure in expansive regions of the mantle (e.g., *Neele et al.*, 1997; *Zhao and Chevrot*, 2003) and the modeling may be complicated by interference with core phases (*Koroni et al.*, 2017). The sensitivity kernels of ScS_2 and the corresponding bottom-side reflection at the 660 (i.e., $ScS_{660}ScS$) shown in Figure 4.11 are similarly broad and complex.

Our modeling of synthetic waveforms for 3-D models of the mantle confirm that structure throughout the mantle affects the propagation of multiple ScS waves. The resolved image for tomographic model S20RTS has a thinner average MTZ because of the elevated shear velocity within the MTZ beneath the western Pacific region. The thickness perturbations are 5 km, which is roughly a third of the variation seen in the waveform data image. This demonstrates that shear-velocity heterogeneity in the mantle is projected as relatively strong topography on the 410 and and 660. Although not illustrated in this paper, we have found that ray-theoretical corrections for traveltime perturbation due to S20RTS structure

in the upper mantle do not remove the projected topography.

Our analysis of synthetics for model PREM-D suggest that ScS reverberations are less sensitive to degree-20 scale perturbations of the MTZ thickness. Whereas in PREM-D the thickness of the MTZ varies by as much as 30 km, the variation in the resolved image is about 5 km, only slightly larger than the 4-km intrinsic uncertainty of the migration method.

While our synthetic tests for two models cannot fully characterize the modeling artifacts, it appears that shear-velocity structure affects long-period ScS reverberation traveltimes more than topography on the 410 and 660 at horizontal degree-20 horizontal scales. It is therefore valid to question the quality of the data images from Figures 4.4 and 4.5. This migration would benefit from traveltime correction due to global-scale velocity structure or from joint analyses of 410 and 660 topography and shear-velocity structure based on a modeling approach that accounts for the broad sensitivities of multiple ScS waves to velocity structure and on high-resolution shear-velocity models of the mantle (e.g., *Chen et al.*, 2015).

No.	Lat	Lon	Time (UTC)	Depth (km)	Mw
1	7.23S	123.04E	2017-10-24 10:47:47	549	6.7
2	27.78N	139.80E	2017-09-07 17:26:49	451	6.1
3	9.38N	123.95E	2017-05-20 01:06:14	533	6.0
4	4.46N	122.57E	2017-01-10 06:13:47	612	7.3
5	7.31S	123.38E	2016-12-05 01:13:04	526	6.3
6*	4.86N	108.16E	2016-10-19 00:26:01	614	6.6
7	24.94N	142.01E	2016-08-04 16:24:33	510	6.3
8	21.97S	178.20E	2016-05-28 05:38:50	405	6.9
9*	23.09N	94.87 E	2016-04-13 13:55:17	136	6.9
10	36.52N	70.36 E	2015-10-26 09:09:42	231	7.5
11	27.83N	140.49E	2015-05-30 11:23:02	664	7.8
12	25.54N	122.45E	2014-12-10 21:03:39	256	6.1
13	28.39N	138.87E	2014-06-30 19:55:33	527	6.2
14	27.42N	127.32E	2014-03-02 20:11:22	118	6.5
15	4.64N	123.40E	2013-11-03 11:03:40	556	6.0
16	12.27N	141.71E	2013-10-06 16:38:10	118	6.0
17*	53.14N	152.90E	2013-10-01 03:38:21	578	6.7
18*	52.14N	151.57E	2013-05-24 14:56:31	632	6.7
19*	18.77N	145.29E	2013-05-14 00:32:26	611	6.8
20	42.73N	131.06E	2013-04-05 13:00:02	571	6.3
21*	42.78N	143.15E	2013-02-02 14:17:34	105	6.9
22*	49.75N	145.31E	2012-08-14 02:59:38	590	7.7
23*	5.53S	147.43E	2012-04-17 07:13:49	208	6.9
24*	7.56S	146.80E	2011-12-14 05:04:17	128	7.1
25	6.36S	126.75E	2011-08-30 06:57:41	467	6.9
26*	26.98N	139.87E	2011-01-12 21:32:54	524	6.5
27*	6.56N	123.36E	2010-07-29 07:31:56	615	6.6
28	6.711N	123.48E	2010-07-23 22:08:11	610	7.3
29	19.35N	144.75E	2010-03-08 09:47:10	446	6.1
30*	42.59N	130.70E	2010-02-18 01:13:19	578	6.9
31	17.24S	178.45E	2009-11-09 10:44:54	591	7.3
32	6.11S	130.42E	2009-10-24 14:40:44	140	6.3
33	4.08N	122.53E	2009-10-07 21:41:14	586	6.8

34	6.67N	123.50E	2009-10-04 10:58:00	635	6.6
35*	7.20S	123.46E	2009-08-28 01:51:19	640	6.9
36	33.14N	138.05E	2009-08-09 10:55:56	302	7.1

Table 4.1: Table of events used in data analysis. Asterisks indicate events included in simulations.

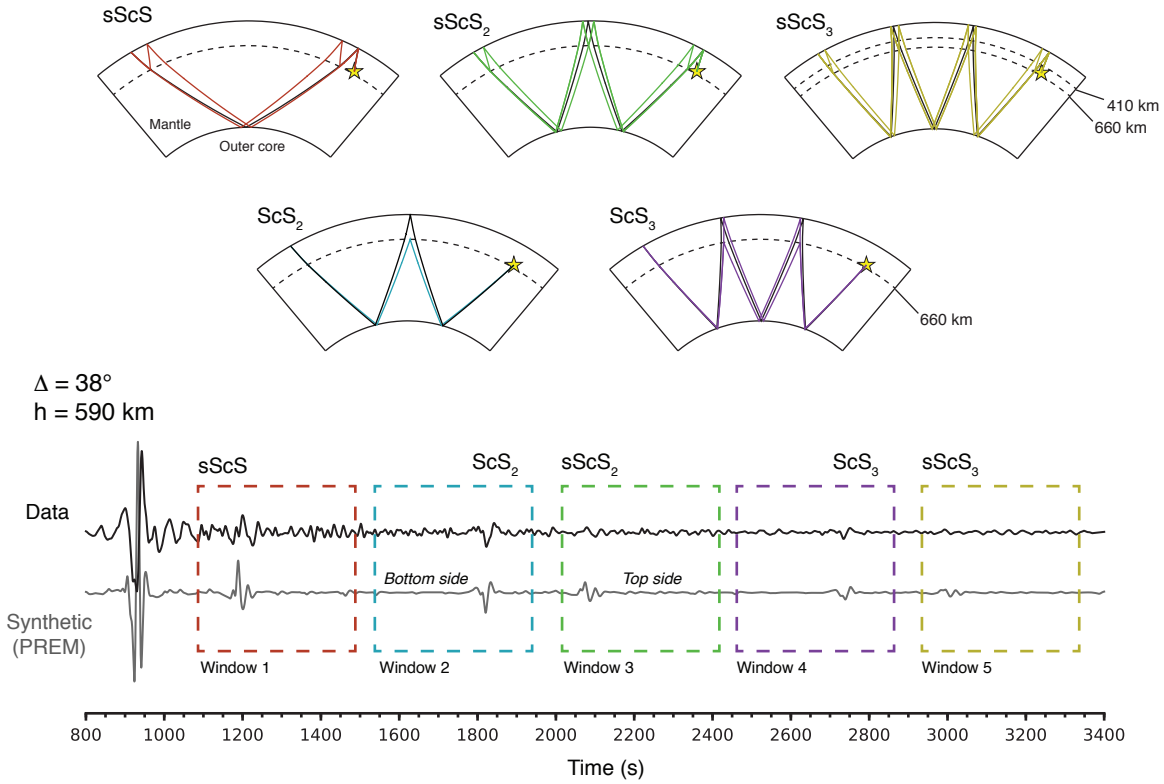

Figure 4.1: (top) Ray diagrams of the five main ScS multiples and corresponding reverberations for an epicentral distance of 60°. (bottom) Transverse-component recording and PREM synthetic of the 2012-08-04 Okhotsk earthquake (Event 22; depth = 590 km; M_W = 7.7) at station CB.GYA at a distance of 38°. In this recording, the ScS reverberations considered in this study arrive between 1100 s and 3400 s. The dashed squares indicate the reverberation windows 1, 2, 3, 4, and 5.

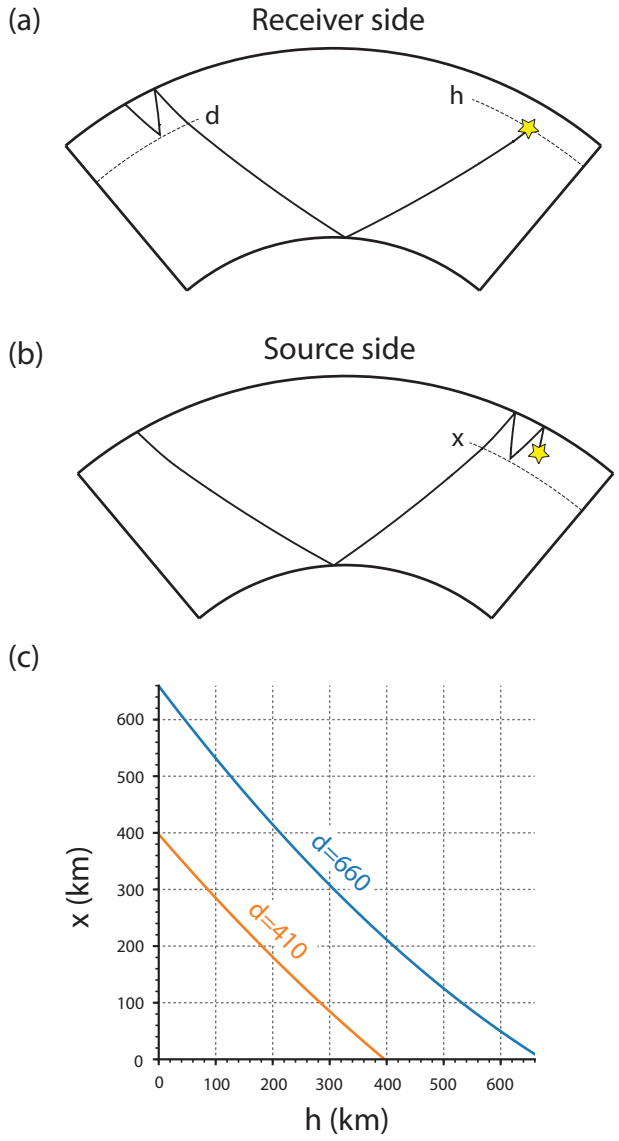

Figure 4.2: Illustration of the traveltime degeneracy between (a) the topside reflection off the 660, $ScSS_{660}S$ and (b) the topside reflection off a discontinuity at depth x, sS_xSScS for an earthquake at depth h. (c) indicates values for h and x when the traveltimes of sS_xSScS and $ScSS_{660}S$ (blue) and of sS_xSScS and $ScSS_{410}S$ (orange) are the same.

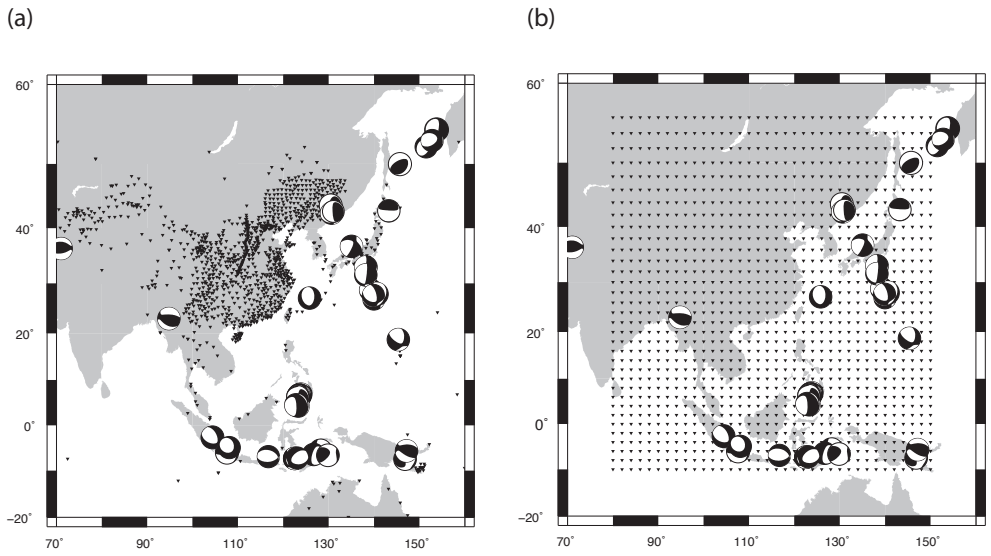

Figure 4.3: Maps of the study region with earthquake locations and mechanisms (shown as 'beach ball diagrams') and locations of stations (triangles) in (a) the Arrays of China, Hinet, and GSN used to analyze recorded waveforms and (b) a rectangular grid used to explore imaging artefacts.

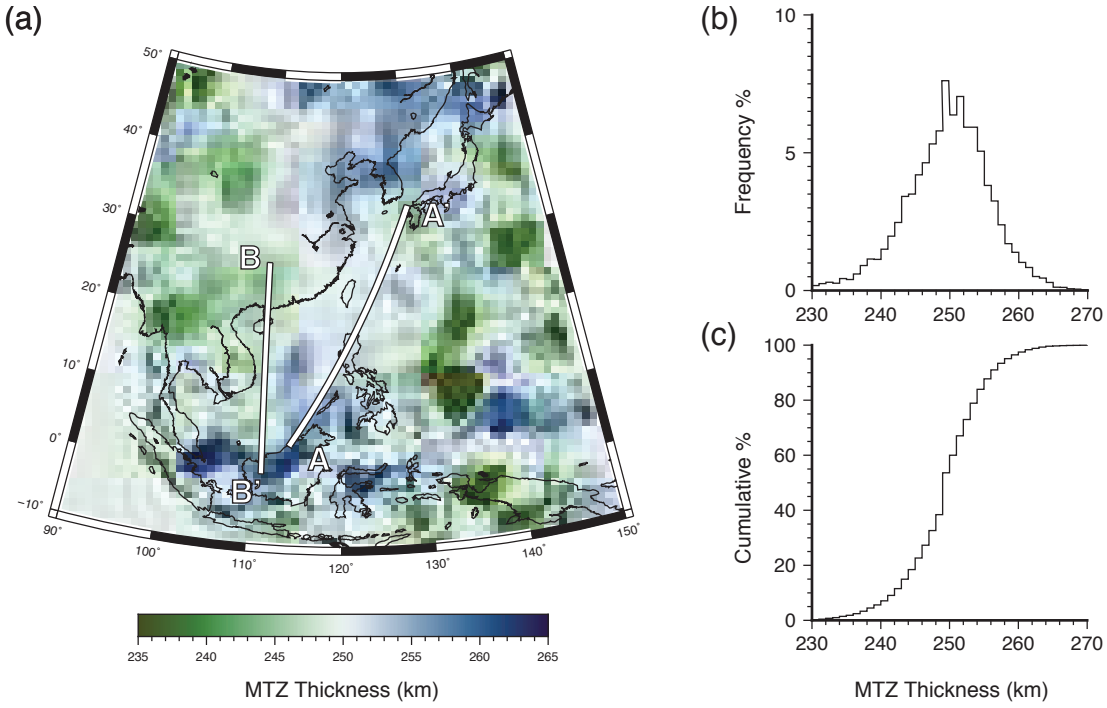

Figure 4.4: (a) Map of the resolved thickness of the MTZ for data from events in Table 1. (b and c) Frequency and cumulative histograms of the resolved MTZ thickness values.

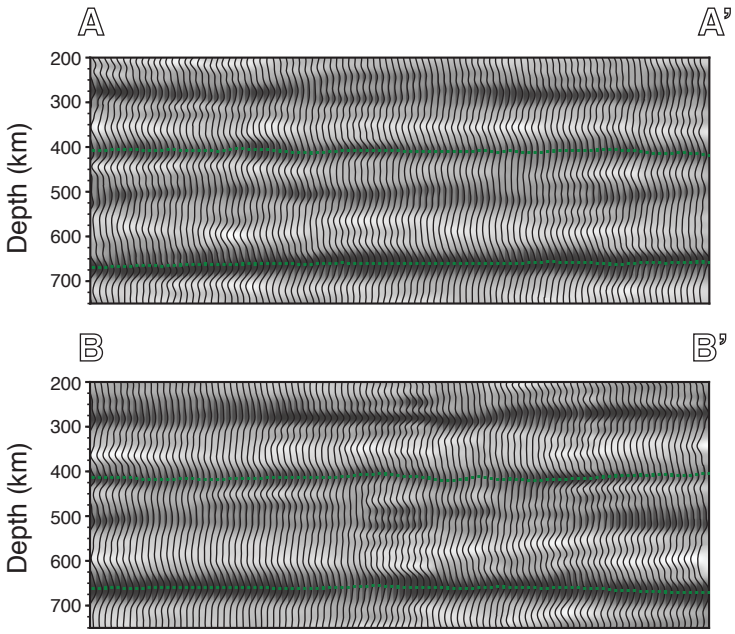

Figure 4.5: Cross sections through the common reflection point image along the transects A–A' and B–B' drawn in Figure 4.4.

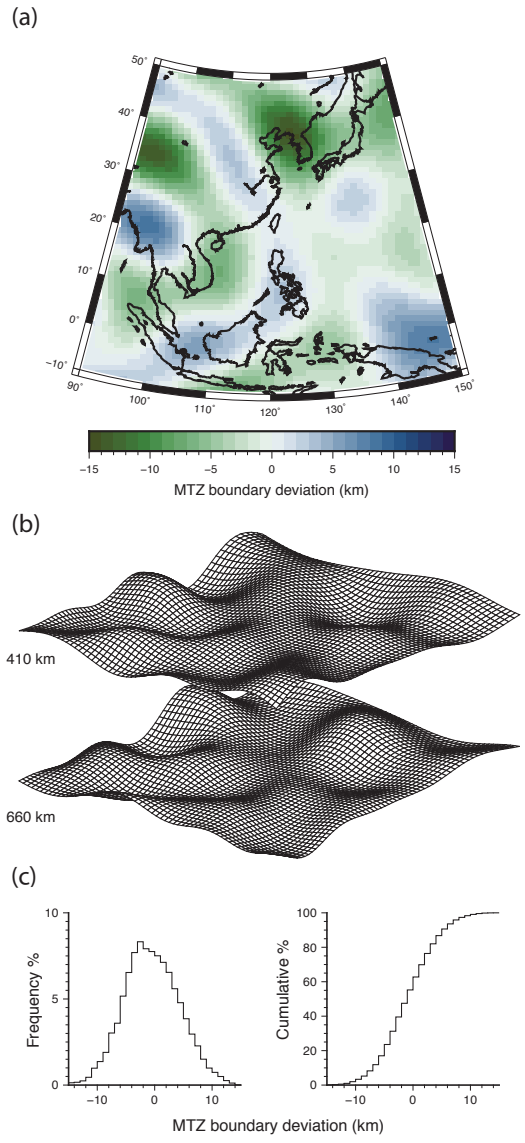

Figure 4.6: (a) Map and (b) surface rendering view of the opposite topography on the 410 and 660 boundaries prescribed in model PREM-D. (c) Frequency and cumulative histograms of the prescribed thickness of the MTZ shown in (a) and (b).

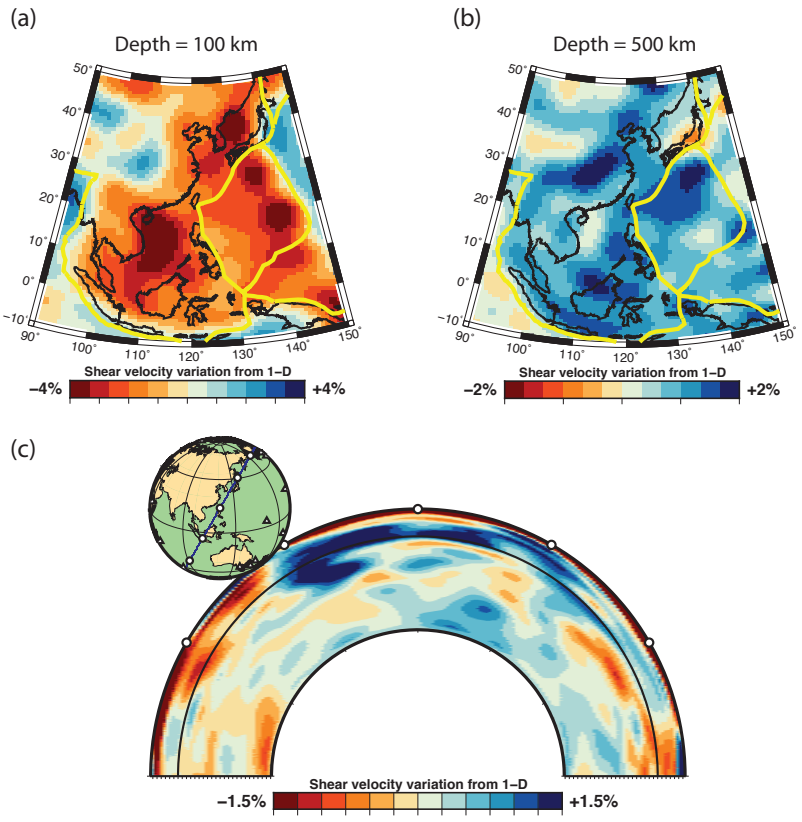

Figure 4.7: Map-view of the shear-velocity structure of model PREM-V at (a) 100 km depth and (b) 500 km depth. (c) Cross-sectional view of PREM-V along the A–A' transect of figure 4.4.

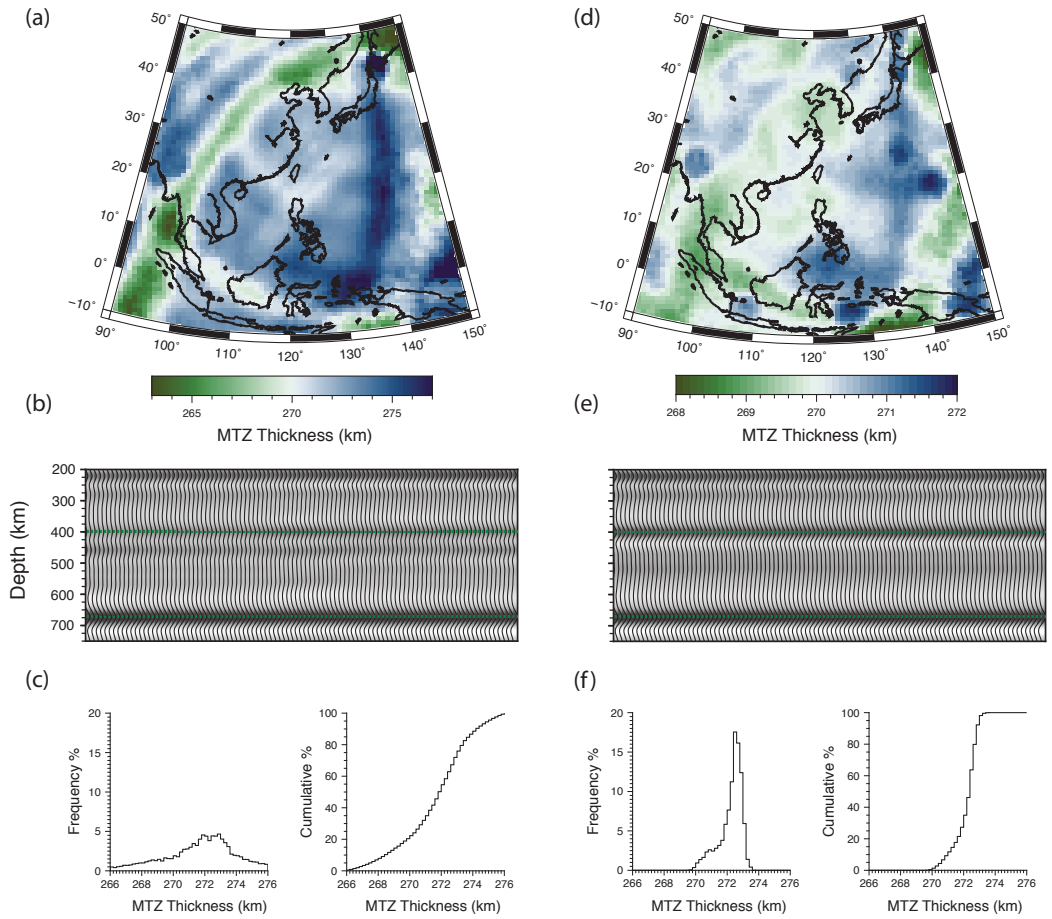

Figure 4.8: (a) Recovered MTZ thickness maps for PREM simulations from earthquakes in Table 1 denoted by asterisks. (d) includes only earthquakes deeper than 220 km. Panels (b) and (e) are cross sections from the common-reflection-point image along the A–A' transect of figure 4.4. Panels (c) and (f) are percent and cumulative percent histograms of the MTZ thickness.

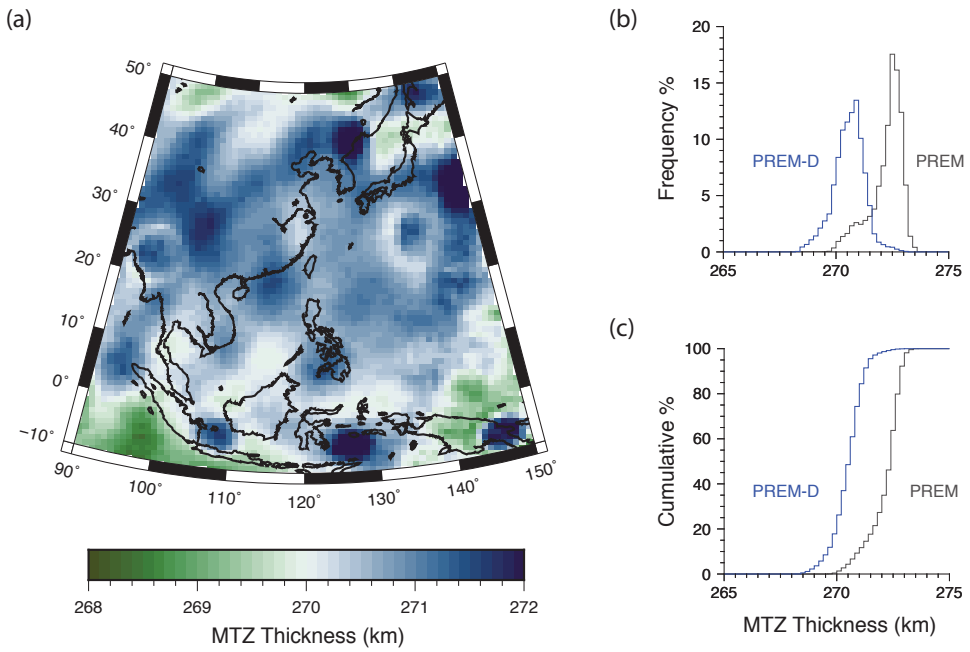

Figure 4.9: (a) Resolved MTZ thickness obtained by migrating the waveforms for model PREM-D. (b) Frequency and (c) cumulative histograms of the estimated MTZ thickness for models PREM (in grey) (see Figure 4.8) and PREM-D (in blue) shown in (a).

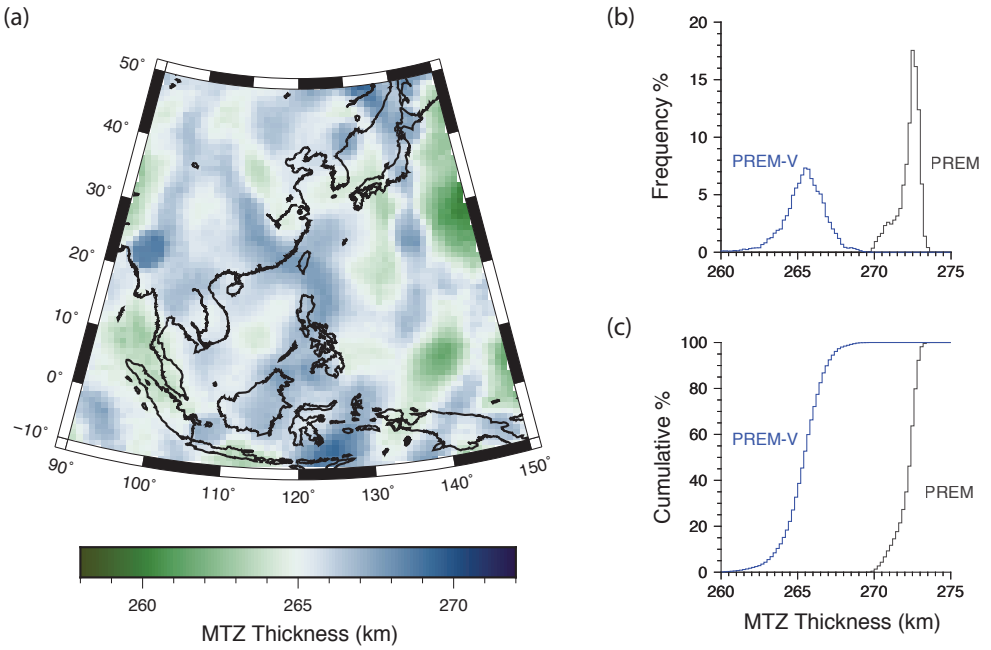

Figure 4.10: (a) Resolved MTZ thickness obtained by migrating the waveforms for model PREM-V. (b) Frequency and (c) cumulative histograms of the estimated MTZ thickness for models PREM (in grey) (see Figure 4.8) and PREM-V (in blue) shown in (a).

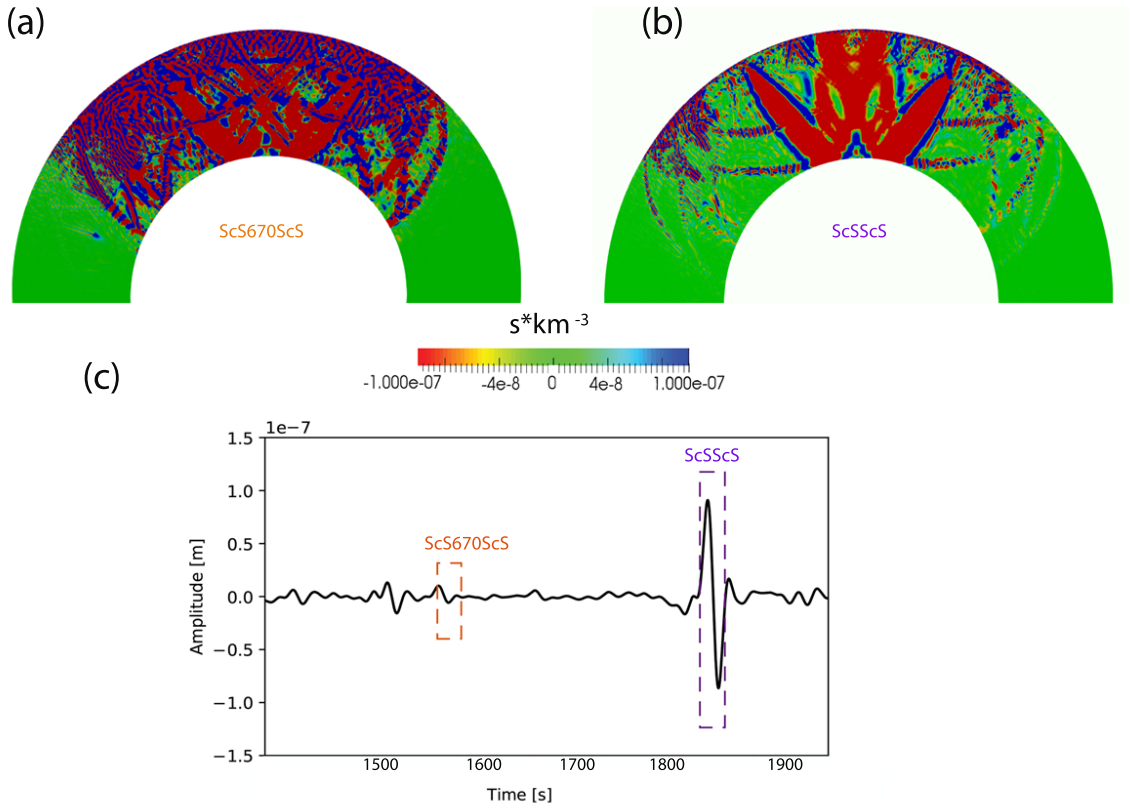

Figure 4.11: Traveltime sensitivity kernels computed with the adjoint method for (a) $ScS_{660}ScS$ and (b) ScSScS calculated using the PREM synthetic shown in (c) for an earthquake at 620 km depth, an epicentral distance of 49°, and a period of 15 s. The squares indicate the 40-second wide segments around $ScS_{660}ScS$ and ScSScS used in the kernel calculations of (a & b).

CHAPTER 5

Conclusions

The work compiled in this dissertation describes how methods of global seismology augmented with geodynamics, geochemistry, and mineral physics provide insight into the composition, distribution, and scale of small scale heterogeneity in Earth's mantle. In addition, we tested the ability of the ScS reverberation migration method to resolve the MTZ thickness.

In chapter 2, I investigated a S-P conversion due to a localized heterogeneity 1750 km beneath Western Brazil recorded at the broadband US Array. I modeled the heterogeneity as a block in the mid-mantle, with variable thickness and velocity contrast. Using finite-difference synthetics, I found that the recorded signal was consistent with an S-P conversion from a 10 km thick block with a shear velocity between 1.6% to 12.4% slower than the surrounding mantle. While the uncertainty in elasticity contrast is large due to the variability in signal amplitude, the signal polarity indicates that the heterogeneity has a slower shear velocity than the surrounding mantle. The low velocity estimate is consistent with the expected shear softening of the stishovite to the $CaCl_2$ structure of silica.

In chapter 3, I investigated whether PKIKP precursors could be explained by geodynamically constructed eclogite profiles in the lower mantle. I modeled the global PKIKP precursor envelope as scattering of PKP waves in the lower mantle due to these profiles. This study was the first to model PKP scattering using a combined geodynamic/full-waveform approach. The results confirmed that subducted eclogite accumulating at the core-mantle boundary may explain the origin of PKIKP precursors.

In chapter 4, I use data from 36 earthquakes beneath Indonesia, the Philippine Sea, and the Sea of Okhotsk recorded by the Arrays of China, Hi-NET, and the Global Seismic Network to study the mantle transition zone beneath the western Pacific. I used the method of ScS reverberation migration to make ray theoretical common reflection point (CRP) stacks of the mid mantle beneath China and its surrounding regions. From these CRP stacks, I was able to measure the MTZ thickness across mainland China and its surrounding oceans.

While results from the data migration reveal MTZ thickness variations that correlate with locations of subducted slabs, synthetic tests showed that processing artefacts that strongly influence the recovered MTZ thickness. By reproducing the method with spectral element synthetics computed for Earth models with 3-D velocity heterogeneities and degree-20 topography on the 410 and 660, I found that velocity heterogeneity strongly influences the recovered MTZ thickness. In addition, the broad sensitivity kernels of the ScS reverberations at 15 s periods render degree-20 topography unrecoverable.

The research presented in this dissertation synthesizes the fields of geochemistry, geodynamics, mineral physics, and seismology. Chapters 2 and 3 relied on using advanced computational resources in order simulate the high frequencies needed to resolve kilometer-scale structure in the deep mantle. These studies were only computationally feasible by assuming in–plane wave propagation and axisymmetric velocity models. Future advances in computational resources will allow us to explore more realistic velocity models and account for out-of-plane scattering and conversions. Chapter 4 exposed the limitations of using ray-theoretical migration methods on long-period seismic phases. These phases have broad sensitivity kernels and need to be analyzed with a finite-frequency theory that is computationally unfeasible.

The greatest limitation to computational seismology is the computational cost of simulating high-frequency phases and treating low-frequency phases with the proper theory. Future studies may be able to further constrain the heterogeneity structure in the lower mantle by incorporating a wider suite of geodynamic models, off-azimuth scattering, and higher frequencies. Advances in computational science will allow us to simulate higher frequencies for fully 3-D wave propagation. All of these computational advances will allow us to explore a larger model space of deep Earth compositions and structures and bring us closer to an understanding of Earth's mantle that is consistent with multiple fields of study.

BIBLIOGRAPHY

Ai, Y., T. Zheng, W. Xu, Y. He, and D. Dong (2003), A complex 660 km discontinuity beneath northeast China, *Earth and Planetary Science Letters*, *212*(1-2), 63–71.

Aki, K., and B. Chouet (1975), Origin of coda waves: source, attenuation, and scattering effects, *Journal of Geophysical Research*, *80*(23), 3322–3342.

Bagley, B., A. M. Courtier, and J. Revenaugh (2013), Seismic shear wave reflectivity structure of the mantle beneath northeast China and the northwest Pacific, *Journal of Geophysical Research: Solid Earth*, *118*(10), 5417–5427.

Bai, L., Y. Zhang, and J. Ritsema (2012), An analysis of SS precursors using spectral-element method seismograms, *Geophysical Journal International*, *188*(1), 293–300.

Bataille, K., and S. M. Flatté (1988), Inhomogeneities near the core-mantle boundary inferred from short-period scattered PKP waves recorded at the Global Digital Seismograph Network, *Journal of Geophysical Research: Solid Earth*, *93*(B12), 15,057–15,064.

Bolfan-Casanova, N., D. Andrault, E. Amiguet, and N. Guignot (2009), Equation of state and post-stishovite transformation of al-bearing silica up to 100 GPa and 3000 K, *Physics of the Earth and Planetary Interiors*, *174*(1-4), 70–77.

Brandenburg, J., E. H. Hauri, P. E. van Keken, and C. J. Ballentine (2008), A multiple-system study of the geochemical evolution of the mantle with force-balanced plates and thermochemical effects, *Earth and Planetary Science Letters*, *276*(1-2), 1–13.

Cao, A., and B. Romanowicz (2007), Locating scatterers in the mantle using array analysis of PKP precursors from an earthquake doublet, *Earth and Planetary Science Letters*, *255*(1-2), 22–31.

Castle, J. C., and R. D. Van Der Hilst (2003), Searching for seismic scattering off mantle interfaces between 800 km and 2000 km depth, *Journal of Geophysical Research: Solid Earth*, *108*(B2).

Chambers, K., A. Deuss, and J. Woodhouse (2005), Reflectivity of the 410-km discontinuity from pp and ss precursors, *Journal of Geophysical Research: Solid Earth*, *110*(B2).

Chaves, C. A., and J. Ritsema (2016), The influence of shear-velocity heterogeneity on ScS2/ScS amplitude ratios and estimates of Q in the mantle, *Geophysical Research Letters*, *43*(15), 7997–8005.

Chen, M., F. Niu, Q. Liu, J. Tromp, and X. Zheng (2015), Multiparameter adjoint tomography of the crust and upper mantle beneath East Asia: 1. Model construction and comparisons, *Journal of Geophysical Research: Solid Earth*, *120*(3), 1762–1786.

Chernov, L. A., and R. A. Silverman (1960), *Wave propagation in a random medium*, New York: McGraw-Hill.

Cleary, J., and R. Haddon (1972), Seismic wave scattering near the core-mantle boundary: a new interpretation of precursors to PKP, *Nature*, *240*(5383), 549.

Cobden, L., S. Goes, M. Ravenna, E. Styles, F. Cammarano, K. Gallagher, and J. A. Connolly (2009), Thermochemical interpretation of 1-D seismic data for the lower mantle: The significance of nonadiabatic thermal gradients and compositional heterogeneity, *Journal of Geophysical Research: Solid Earth*, *114*(B11).

Cormier, V. F. (1999), Anisotropy of heterogeneity scale lengths in the lower mantle from PKIKP precursors, *Geophysical Journal International*, *136*(2), 373–384.

Courtier, A. M., and J. Revenaugh (2006), A water-rich transition zone beneath the eastern United States and Gulf of Mexico from multiple ScS reverberations, *Geophysical Monograph-American Geophysical Union*, *168*, 181.

Courtier, A. M., and J. Revenaugh (2007), Deep upper-mantle melting beneath the Tasman and Coral Seas detected with multiple ScS reverberations, *Earth and Planetary Science Letters*, *259*(1-2), 66–76.

Crotwell, H. P., T. J. Owens, and J. Ritsema (1999), The TauP Toolkit: Flexible seismic travel-time and ray-path utilities, *Seismological Research Letters*, *70*, 154–160.

Day, E. A., and A. Deuss (2013), Reconciling PP and P'P' precursor observations of a complex 660 km seismic discontinuity, *Geophysical Journal International*, *194*(2), 834–838.

Deuss, A. (2009), Global observations of mantle discontinuities using SS and PP precursors, *Surveys in geophysics*, *30*(4-5), 301–326.

Deuss, A., and J. Woodhouse (2001), Seismic observations of splitting of the mid-transition zone discontinuity in Earth's mantle, *Science*, *294*(5541), 354–357.

Doornbos, D. (1978), On seismic-wave scattering by a rough core–mantle boundary, *Geophysical Journal International*, *53*(3), 643–662.

Doornbos, D., and E. Husebye (1972), Array analysis of PKP phases and their precursors, *Physics of the Earth and Planetary Interiors*, *5*, 387–399.

Earle, P. S., and P. M. Shearer (1997), Observations of PKKP precursors used to estimate small-scale topography on the core-mantle boundary, *Science*, *277*(5326), 667–670.

Earle, P. S., and P. M. Shearer (2001), Distribution of fine-scale mantle heterogeneity from observations of Pdiff coda, *Bulletin of the Seismological Society of America*, *91*(6), 1875–1881.

Flanagan, M. P., and P. M. Shearer (1998), Global mapping of topography on transition zone velocity discontinuities by stacking SS precursors, *Journal of Geophysical Research: Solid Earth*, *103*(B2), 2673–2692.

Frost, D. A., S. Rost, N. D. Selby, and G. W. Stuart (2013), Detection of a tall ridge at the core–mantle boundary from scattered PKP energy, *Geophysical Journal International*, *195*(1), 558–574.

Fukao, Y., S. Widiyantoro, and M. Obayashi (2001), Stagnant slabs in the upper and lower mantle transition region, *Reviews of Geophysics*, *39*(3), 291–323.

Gao, Y., D. Suetsugu, Y. Fukao, M. Obayashi, Y. Shi, and R. Liu (2010), Seismic discontinuities in the mantle transition zone and at the top of the lower mantle beneath eastern China and Korea: Influence of the stagnant Pacific slab, *Physics of the Earth and Planetary Interiors*, *183*(1-2), 288–295.

Grand, S. P., and D. V. Helmberger (1984), Upper mantle shear structure of North America, *Geophysical Journal International*, *76*(2), 399–438.

Grand, S. P., R. D. van der Hilst, and S. Widiyantoro (1997), High resolution global tomography: a snapshot of convection in the Earth, *Geological Society of America Today*, *7*(4).

Haddon, R., and J. Cleary (1974), Evidence for scattering of seismic PKP waves near the mantle-core boundary, *Physics of the Earth and Planetary Interiors*, *8*(3), 211–234.

Haddon, R., E. Husebye, and D. King (1977), Origins of precursors to P'P', *Physics of the Earth and Planetary Interiors*, *14*(1), 41–70.

Hedlin, M. A., and P. M. Shearer (2000), An analysis of large-scale variations in small-scale mantle heterogeneity using Global Seismographic Network recordings of precursors to PKP, *Journal of Geophysical Research: Solid Earth*, *105*(B6), 13,655–13,673.

Hedlin, M. A., P. M. Shearer, and P. S. Earle (1997), Seismic evidence for small-scale heterogeneity throughout the Earth's mantle, *Nature*, *387*(6629), 145.

Hirose, K., Y. Fei, Y. Ma, and H.-K. Mao (1999), The fate of subducted basaltic crust in the Earth's lower mantle, *Nature*, *397*(6714), 53.

Hwang, Y. K., J. Ritsema, P. E. van Keken, S. Goes, and E. Styles (2011), Wavefront healing renders deep plumes seismically invisible, *Geophysical Journal International*, *187*(1), 273–277.

Irifune, T., and A. Ringwood (1987), Phase transformations in a harzburgite composition to 26 GPa: implications for dynamical behaviour of the subducting slab, *Earth and Planetary Science Letters*, *86*(2-4), 365–376.

Irifune, T., and A. Ringwood (1993), Phase transformations in subducted oceanic crust and buoyancy relationships at depths of 600–800 km in the mantle, *Earth and Planetary Science Letters*, *117*(1-2), 101–110.

Irifune, T., and T. Tsuchiya (2015), Phase transitions and mineralogy of the lower mantle.

Jahnke, G., M. S. Thorne, A. Cochard, and H. Igel (2008), Global SH-wave propagation using a parallel axisymmetric spherical finite-difference scheme: application to whole mantle scattering, *Geophysical Journal International*, *173*(3), 815–826.

Jenkins, J., S. Cottaar, R. S. White, and A. Deuss (2016), Depressed mantle discontinuities beneath Iceland: Evidence of a garnet controlled 660 km discontinuity?, *Earth and Planetary Science Letters*, *433*, 159–168.

Kaneshima, S. (2013), Lower mantle seismic scatterers below the subducting Tonga slab: Evidence for slab entrainment of transition zone materials, *Physics of the Earth and Planetary Interiors*, *222*, 35–46.

Kaneshima, S. (2016), Seismic scatterers in the mid-lower mantle, *Physics of the Earth and Planetary Interiors*, *257*, 105–114.

Kaneshima, S., and G. Helffrich (1998), Detection of lower mantle scatterers northeast of the Marianna subduction zone using short-period array data, *Journal of Geophysical Research: Solid Earth*, *103*(B3), 4825–4838.

Kaneshima, S., and G. Helffrich (1999), Dipping low-velocity layer in the mid-lower mantle: evidence for geochemical heterogeneity, *Science*, *283*(5409), 1888–1892.

Kaneshima, S., and G. Helffrich (2003), Subparallel dipping heterogeneities in the mid-lower mantle, *Journal of Geophysical Research: Solid Earth*, *108*(B5).

Kaneshima, S., and G. Helffrich (2010), Small scale heterogeneity in the mid-lower mantle beneath the circum-pacific area, *Physics of the Earth and Planetary Interiors*, *183*(1-2), 91–103.

Karki, B. B., L. Stixrude, and J. Crain (1997), Ab initio elasticity of three high-pressure polymorphs of silica, *Geophysical Research Letters*, *24*(24), 3269–3272.

Katzman, R., L. Zhao, and T. H. Jordan (1998), High-resolution, two-dimensional vertical tomography of the central Pacific mantle using ScS reverberations and frequency-dependent travel times, *Journal of Geophysical Research: Solid Earth*, *103*(B8), 17,933–17,971.

Kawai, K., and T. Tsuchiya (2012), Phase stability and elastic properties of the NAL and CF phases in the $NaMg_2Al_5SiO_{12}$ system from first principles, *American Mineralogist*, *97*(2-3), 305–314.

Kawakatsu, H., and F. Niu (1994), Seismic evidence for a 920-km discontinuity in the mantle, *Nature*, *371*(6495), 301.

Kind, R. (2007), Deep earth structure–Transition zone and mantle discontinuities, *Treatise on Geophysics, 1, Seismology and Structure of the Earth*, pp. 591–618.

King, D., E. Husebye, and R. Haddon (1976), Processing of seismic precursor data, *Physics of the Earth and Planetary Interiors*, *12*(2-3), 128–134.

Komatitsch, D., and J. Tromp (2002), Spectral-element simulations of global seismic wave propagation–I. Validation, *Geophysical Journal International*, *149*(2), 390–412.

Koroni, M., and J. Trampert (2015), The effect of topography of upper-mantle discontinuities on SS precursors, *Geophysical Journal International*, *204*(1), 667–681.

Koroni, M., E. Bozdağ, H. Paulssen, and J. Trampert (2017), Sensitivity analysis of seismic waveforms to upper-mantle discontinuities using the adjoint method, *Geophysical Journal International*, *210*(3), 1965–1980.

Kudo, Y., K. Hirose, M. Murakami, Y. Asahara, H. Ozawa, Y. Ohishi, and N. Hirao (2012), Sound velocity measurements of $CaSiO_3$ perovskite to 133 GPa and implications for lowermost mantle seismic anomalies, *Earth and Planetary Science Letters*, *349*, 1–7.

Labrosse, S., J. Hernlund, and N. Coltice (2007), A crystallizing dense magma ocean at the base of the Earth's mantle, *Nature*, *450*(7171), 866.

Lakshtanov, D. L., S. V. Sinogeikin, K. D. Litasov, V. B. Prakapenka, H. Hellwig, J. Wang, C. Sanches-Valle, J.-P. Perrillat, B. Chen, M. Somayazulu, et al. (2007), The post-stishovite phase transition in hydrous alumina-bearing SiO_2 in the lower mantle of the Earth, *Proceedings of the National Academy of Sciences*, *104*(34), 13,588–13,590.

Lawrence, J. F., and P. M. Shearer (2006), A global study of transition zone thickness using receiver functions, *Journal of Geophysical Research: Solid Earth*, *111*(B6).

Leng, K., T. Nissen-Meyer, and M. van Driel (2016), Efficient global wave propagation adapted to 3-D structural complexity: a pseudospectral/spectral-element approach, *Geophysical Supplements to the Monthly Notices of the Royal Astronomical Society*, *207*(3), 1700–1721.

Li, J., and D. A. Yuen (2014), Mid-mantle heterogeneities associated with Izanagi plate: Implications for regional mantle viscosity, *Earth and Planetary Science Letters*, *385*, 137–144.

Li, X., and X. Yuan (2003), Receiver functions in northeast China–implications for slab penetration into the lower mantle in northwest Pacific subduction zone, *Earth and Planetary Science Letters*, *216*(4), 679–691.

Litasov, K., E. Ohtani, A. Suzuki, T. Kawazoe, and K. Funakoshi (2004), Absence of density crossover between basalt and peridotite in the cold slabs passing through 660 km discontinuity, *Geophysical Research Letters*, *31*(24).

Maguire, R., J. Ritsema, P. E. van Keken, A. Fichtner, and S. Goes (2016), P-and S-wave delays caused by thermal plumes, *Geophysical Journal International*, *206*(2), 1169–1178.

Maguire, R., J. Ritsema, and S. Goes (2017), Signals of 660 km topography and harzburgite enrichment in seismic images of whole-mantle upwellings, *Geophysical Research Letters*, *44*(8), 3600–3607.

Mancinelli, N., P. Shearer, and C. Thomas (2016), On the frequency dependence and spatial coherence of PKP precursor amplitudes, *Journal of Geophysical Research: Solid Earth*, *121*(3), 1873–1889.

Mancinelli, N. J., and P. M. Shearer (2013), Reconciling discrepancies among estimates of small-scale mantle heterogeneity from PKP precursors, *Geophysical Journal International*, *195*(3), 1721–1729.

Margerin, L., and G. Nolet (2003), Multiple scattering of high-frequency seismic waves in the deep Earth: PKP precursor analysis and inversion for mantle granularity, *Journal of Geophysical Research: Solid Earth*, *108*(B11).

Miller, M. S., and F. Niu (2008), Bulldozing the core–mantle boundary: Localized seismic scatterers beneath the Caribbean Sea, *Physics of the Earth and Planetary Interiors*, *170*(1-2), 89–94.

Neele, F., H. de Regt, and J. Van Decar (1997), Gross errors in upper-mantle discontinuity topography from underside reflection data, *Geophysical Journal International*, *129*(1), 194–204.

Nissen-Meyer, T., M. v. Driel, S. Stähler, K. Hosseini, S. Hempel, L. Auer, A. Colombi, and A. Fournier (2014), AxiSEM: broadband 3-D seismic wavefields in axisymmetric media, *Solid Earth*, (1), 425–445.

Niu, F. (2014), Distinct compositional thin layers at mid-mantle depths beneath northeast China revealed by the USArray, *Earth and Planetary Science Letters*, *402*, 305–312.

Niu, F., and H. Kawakatsu (1996), Complex structure of mantle discontinuities at the tip of the subducting slab beneath northeast China, *Journal of Physics of the Earth*, *44*(6), 701–711.

Niu, F., and L. Wen (2001), Strong seismic scatterers near the core-mantle boundary west of Mexico, *Geophysical research letters*, *28*(18), 3557–3560.

Nomura, R., K. Hirose, N. Sata, and Y. Ohishi (2010), Precise determination of post-stishovite phase transition boundary and implications for seismic heterogeneities in the mid-lower mantle, *Physics of the Earth and Planetary Interiors*, *183*(1-2), 104–109.

Ohtaki, T., D. Suetsugu, K. Kanjo, and I. Purwana (2002), Evidence for a thick mantle transition zone beneath the Philippine Sea from multiple-ScS waves recorded by JISNET, *Geophysical research letters*, *29*(13).

Ono, S., K. Hirose, M. Murakami, and M. Isshiki (2002), Post-stishovite phase boundary in SiO_2 determined by in situ X-ray observations, *Earth and Planetary Science Letters*, *197*(3-4), 187–192.

Revenaugh, J., and T. H. Jordan (1989), A study of mantle layering beneath the western Pacific, *Journal of Geophysical Research: Solid Earth*, *94*(B5), 5787–5813.

Revenaugh, J., and S. Sipkin (1994), Seismic evidence for silicate melt atop the 410-km mantle discontinuity, *Nature*, *369*(6480), 474.

Ricolleau, A., J.-P. Perrillat, G. Fiquet, I. Daniel, J. Matas, A. Addad, N. Menguy, H. Cardon, M. Mezouar, and N. Guignot (2010), Phase relations and equation of state of a natural MORB: Implications for the density profile of subducted oceanic crust in the Earth's lower mantle, *Journal of Geophysical Research: Solid Earth*, *115*(B8).

Ritsema, J., a. A. Deuss, H. Van Heijst, and J. Woodhouse (2011), S40RTS: a degree-40 shear-velocity model for the mantle from new Rayleigh wave dispersion, teleseismic traveltime and normal-mode splitting function measurements, *Geophysical Journal International*, *184*(3), 1223–1236.

Saita, T., D. Suetsugu, T. Ohtaki, H. Takenaka, K. Kanjo, and I. Purwana (2002), Transition zone thickness beneath Indonesia as inferred using the receiver function method for data from the JISNET regional broadband seismic network, *Geophysical research letters*, *29*(7).

Schmerr, N., and E. J. Garnero (2007), Upper mantle discontinuity topography from thermal and chemical heterogeneity, *Science*, *318*(5850), 623–626.

Schultz, R., and Y. J. Gu (2013), Flexible, inversion-based Matlab implementation of the Radon transform.

Shearer, P. M. (2007), Seismic scattering in the deep Earth, *Treatise on geophysics*, *1*, 695–730.

Shearer, P. M., M. A. Hedlin, and P. S. Earle (1998), PKP and PKKP precursor observations: Implications for the small-scale structure of the deep mantle and core, *The Core-Mantle Boundary Region, Geodyn. Ser*, *28*, 37–55.

Shen, X., H. Zhou, and H. Kawakatsu (2008), Mapping the upper mantle discontinuities beneath China with teleseismic receiver functions, *Earth, planets and space*, *60*(7), 713–719.

Song, T., and D. V. Helmberger (2006), Low velocity zone atop the transition zone in the western US from S waveform triplication, *Geophysical Monograph-American Geophysical Union*, *168*, 195.

Stähler, S. C., K. Sigloch, and T. Nissen-Meyer (2012), Triplicated P-wave measurements for waveform tomography of the mantle transition zone, *Solid Earth*, *3*(2), 339.

Styles, E., S. Goes, P. E. van Keken, J. Ritsema, and H. Smith (2011), Synthetic images of dynamically predicted plumes and comparison with a global tomographic model, *Earth and Planetary Science Letters*, *311*(3-4), 351–363.

Thomas, C., M. Weber, C. Wicks, and F. Scherbaum (1999), Small scatterers in the lower mantle observed at german broadband arrays, *Journal of Geophysical Research: Solid Earth*, *104*(B7), 15,073–15,088.

Thomas, C., J.-M. Kendall, and G. Helffrich (2009), Probing two low-velocity regions with pkp b-caustic amplitudes and scattering, *Geophysical Journal International*, *178*(1), 503–512.

Thorne, M. S., Y. Zhang, and J. Ritsema (2013), Evaluation of 1-D and 3-D seismic models of the Pacific lower mantle with S, SKS, and SKKS traveltimes and amplitudes, *Journal of Geophysical Research: Solid Earth*, *118*(3), 985–995.

Tkalčić, H., M. P. Flanagan, and V. F. Cormier (2006), Observation of near-podal P'P' precursors: Evidence for back scattering from the 150–220 km zone in the Earth's upper mantle, *Geophysical research letters*, *33*(3).

Tsuchiya, T. (2011), Elasticity of subducted basaltic crust at the lower mantle pressures: Insights on the nature of deep mantle heterogeneity, *Physics of the Earth and Planetary Interiors*, *188*(3-4), 142–149.

Tsuchiya, T., R. Caracas, and J. Tsuchiya (2004), First principles determination of the phase boundaries of high-pressure polymorphs of silica, *Geophysical Research Letters*, *31*(11).

van Driel, M., and T. Nissen-Meyer (2014a), Seismic wave propagation in fully anisotropic axisymmetric media, *Geophysical Journal International*, *199*(2), 880–893.

van Driel, M., and T. Nissen-Meyer (2014b), Optimized viscoelastic wave propagation for weakly dissipative media, *Geophysical Journal International*, *199*(2), 1078–1093.

Van Keken, P. (2001), Cylindrical scaling for dynamical cooling models of the Earth, *Physics of the Earth and Planetary Interiors*, *124*(1-2), 119–130.

Vanacore, E., F. Niu, and H. Kawakatsu (2006), Observations of the mid-mantle discontinuity beneath Indonesia from S to P converted waveforms, *Geophysical research letters*, *33*(4).

Vanacore, E., F. Niu, and Y. Ma (2010), Large angle reflection from a dipping structure recorded as a PKIKP precursor: Evidence for a low velocity zone at the core–mantle boundary beneath the Gulf of Mexico, *Earth and Planetary Science Letters*, *293*(1-2), 54–62.

Vidale, J. E., and P. S. Earle (2000), Fine-scale heterogeneity in the Earth's inner core, *Nature*, *404*(6775), 273.

Vidale, J. E., and M. A. Hedlin (1998), Evidence for partial melt at the core–mantle boundary north of Tonga from the strong scattering of seismic waves, *Nature*, *391*(6668), 682.

Vinnik, L. (1977), Detection of waves converted from P to SV in the mantle, *Physics of the Earth and planetary interiors*, *15*(1), 39–45.

Vinnik, L. (1981), Evaluation of the effective cross-section of scattering in the lithosphere, *Physics of the Earth and Planetary Interiors*, *26*(4), 268–284.

Vinnik, L., F. Niu, and H. Kawakatsu (1998), Broadband converted phases from midmantle discontinuities, *Earth, planets and space*, *50*(11-12), 987–997.

Wang, X., J. Li, and Q.-F. Chen (2017), Topography of the 410 km and 660 km discontinuities beneath the Japan Sea and adjacent regions by analysis of multiple-ScS waves, *Journal of Geophysical Research: Solid Earth*, *122*(2), 1264–1283.

Waszek, L., C. Thomas, and A. Deuss (2015), PKP precursors: Implications for global scatterers, *Geophysical Research Letters*, *42*(10), 3829–3838.

Wen, L. (2000), Intense seismic scattering near the Earth's core-mantle boundary beneath the Comoros hotspot, *Geophysical research letters*, *27*(22), 3627–3630.

Wen, L., and D. V. Helmberger (1998), Ultra-low velocity zones near the core-mantle boundary from broadband PKP precursors, *Science*, *279*(5357), 1701–1703.

Williams, Q., and E. J. Garnero (1996), Seismic evidence for partial melt at the base of Earth's mantle, *Science*, *273*(5281), 1528–1530.

Xu, W., C. Lithgow-Bertelloni, L. Stixrude, and J. Ritsema (2008), The effect of bulk composition and temperature on mantle seismic structure, *Earth and Planetary Science Letters*, *275*(1-2), 70–79.

Yang, Z., and X. He (2015), Oceanic crust in the mid-mantle beneath west-central Pacific subduction zones: evidence from S to P converted waveforms, *Geophysical Journal International*, *203*(1), 541–547.

Yao, J., and L. Wen (2014), Seismic structure and ultra-low velocity zones at the base of the Earths mantle beneath Southeast Asia, *Physics of the Earth and Planetary Interiors*, *233*, 103–111.

Zhao, L., and S. Chevrot (2003), SS-wave sensitivity to upper mantle structure: Implications for the mapping of transition zone discontinuity topographies, *Geophysical research letters*, *30*(11).